

MODELING OF AN ELECTROMAGNETIC LAUNCHER

A THESIS SUBMITTED TO  
THE GRADUATE SCHOOL OF NATURAL AND APPLIED SCIENCES  
OF  
MIDDLE EAST TECHNICAL UNIVERSITY

BY  
YASİN ÇEVİK

IN PARTIAL FULFILLMENT OF THE REQUIREMENTS  
FOR  
THE DEGREE OF MASTER OF SCIENCE  
IN  
ELECTRICAL AND ELECTRONICS ENGINEERING

DECEMBER 2015



Approval of the thesis:

**MODELING OF AN ELECTROMAGNETIC LAUNCHER**

submitted by **YASİN ÇEVİK** in partial fulfillment of the requirements for the degree of **Master of Science in Electrical and Electronics Engineering Department, Middle East Technical University** by,

Prof. Dr. Gülbin Dural Ünver  
Dean, Graduate School of **Natural and Applied Sciences** \_\_\_\_\_

Prof. Dr. Gönül Turhan Sayan  
Head of Department, **Electrical and Electronics Eng.** \_\_\_\_\_

Prof. Dr. Osman Sevaioğlu  
Supervisor, **Electrical and Electronics Eng. Dept., METU** \_\_\_\_\_

Prof. Dr. Mirzahan Hızal  
Co-supervisor, **Electrical and Electronics Eng. Dept., METU** \_\_\_\_\_

**Examining Committee Members:**

Prof. Dr. Muammer Ermiş  
Electrical and Electronics Engineering Dept., METU \_\_\_\_\_

Prof. Dr. Osman Sevaioğlu  
Electrical and Electronics Engineering Dept., METU \_\_\_\_\_

Assoc. Prof. Dr. Nevsan Şengil  
AeEng. Dept., Uni. of Turkish Aeronautical Assoc. \_\_\_\_\_

Assist. Prof. Dr. Murat Göl  
Electrical and Electronics Engineering Dept., METU \_\_\_\_\_

Assist. Prof. Dr. Ozan Keysan  
Electrical and Electronics Engineering Dept., METU \_\_\_\_\_

**Date:** 10/12/2015

**I hereby declare that all information in this document has been obtained and presented in accordance with academic rules and ethical conduct. I also declare that, as required by these rules and conduct, I have fully cited and referenced all material and results that are not original to this work.**

Name, Last name : Yasin Çevik

Signature :

## **ABSTRACT**

### **MODELING OF AN ELECTROMAGNETIC LAUNCHER**

Çevik, Yasin

M.S., Department of Electrical and Electronics Engineering  
Supervisor : Prof. Dr. Osman Sevaioğlu

December 2015, 72 Pages

This thesis involves modeling of an electromagnetic launcher (EML) by taking all of the variables that affect the system performance into consideration. The study includes deriving related electrical and kinematic equations and developing models based on these equations. Two models are built in different simulation programs to be able to analyze the system from different aspects. Models are verified by means of experimental results. An experimental setup is designed and implemented to represent a similar behavior to EML. The same system is simulated using two simulation models. Experimental and simulation results are compared and discussed.

Keywords: Electromagnetic force, electromagnetic launch, modeling, simulation

## ÖZ

### ELEKTROMANYETİK FIRLATICININ MODELLENMESİ

Çevik, Yasin

Yüksek Lisans, Elektrik ve Elektronik Mühendisliği Bölümü  
Tez Yöneticisi : Prof. Dr. Osman Sevaioğlu

Aralık 2015, 72 Sayfa

Bu tez sistem performansını etkileyen tüm değişkenler göz önünde bulundurularak elektromanyetik fırlatıcının modellenmesini içerir. Bu çalışma, ilgili elektriksel ve kinematik denklemlerin çıkarılması ve bu denklemler temel alınarak modellerin geliştirilmesini kapsar. Sistemin farklı açılardan analiz edilebilmesi için farklı benzetim programlarında iki model geliştirilmiştir. Modeller deney sonuçları ile doğrulanmıştır. Elektromanyetik fırlatıcıya benzer bir deney altyapısı tasarlanmış ve kurulmuştur. Aynı sistemin iki modelde de benzetimi yapılarak benzetim sonuçları alınmıştır. Deneysel sonuçlar ve benzetim sonuçları karşılaştırılıp incelenmiştir.

Anahtar Kelimeler: Elektromanyetik kuvvet, elektromanyetik fırlatma, modelleme, benzetim

*to my family and friends ...*

## **ACKNOWLEDGEMENTS**

I would like to express my sincere appreciation to my supervisor Prof. Dr. Osman Sevaioğlu and co-supervisor Prof. Dr. Mirzahan Hızal for his support, guidance and suggestions throughout my thesis study.

I would like to thank my thesis committee members Prof. Dr. Muammer Ermiş, Assoc. Prof. Dr. Nevsan Şengil, Assist. Prof. Dr. Murat Göl and Assist. Prof. Dr. Ozan Keysan for their criticism and advices.

I wish to express my deepest appreciation to my family for their patience and support throughout my life.

I would like to extend special thanks to Anıl Civil, Emre Durna, Emre Kantar, Mert Yıldız and Mustafa Karagöz for their suggestions and significant help to my thesis. I would also like to thank them for their wonderful company and support throughout this study.

I would like to thank my friends Ali Aydoğan, Burak Nurgün, Esra Nurgün, Gökmen Cengiz, Mehmet Aydoğdu and Veysel Yücesoy for their invaluable friendship and support.



## TABLE OF CONTENTS

|  |      |
|--|------|
| ABSTRACT .....   | v    |
| ÖZ.....  | vi   |
| ACKNOWLEDGEMENTS .....                                     | viii |
| TABLE OF CONTENTS .....                                    | ix   |
| LIST OF TABLES .....                                       | xi   |
| LIST OF FIGURES .....                                      | xii  |
| LIST OF ABBREVIATIONS .....                                | xv   |
| 1. INTRODUCTION.....                                       | 1    |
| 1.1. General Information on Electromagnetic Launchers..... | 1    |
| 1.2. Recent EML Research.....                              | 3    |
| 1.2.1. United States of America.....                       | 3    |
| 1.2.2. Europe.....   | 4    |
| 1.2.3. China and Other Asian Countries .....               | 4    |
| 1.3. Purpose of Thesis .....                               | 5    |
| 1.4. Outline of Thesis .....                               | 5    |
| 2. EML BACKGROUND.....                                     | 7    |
| 2.1. Structure of EML.....                                 | 7    |
| 2.1.1. Pulse Forming Unit.....                             | 7    |
| 2.1.2. Conductive Rails.....                               | 10   |
| 2.1.3. Launch Object.....                                  | 10   |
| 2.2. Electromagnetic Launch Theory .....                   | 11   |
| 2.3. Inductance Gradient.....                              | 14   |
| 2.4. Literature Review .....                               | 15   |

|  |    |
|--|----|
| 3. EML MODELING .....                  | 19 |
| 3.1. Electrical Model .....            | 19 |
| 3.1.1. Basic Form of EML .....         | 19 |
| 3.1.2. Multistage EML .....            | 22 |
| 3.2. Kinematic Model .....             | 24 |
| 3.3. Implementation in Simulink .....  | 26 |
| 3.4. Implementation in Simplorer ..... | 32 |
| 4. EXPERIMENTAL PROCEDURE .....        | 45 |
| 4.1. Experimental Goals .....          | 45 |
| 4.2. Experimental Components .....     | 45 |
| 4.3. Data Acquisition .....            | 48 |
| 4.4. Test Procedure and Results .....  | 50 |
| 4.5. Data Analysis .....               | 53 |
| 5. CONCLUSION .....                    | 61 |
| REFERENCES .....                       | 63 |
| APPENDIX A .....                       | 69 |
| APPENDIX B .....                       | 71 |

## LIST OF TABLES

### TABLES

|   |    |
|---|----|
| Table 2.1 Discharge start time for each module .....                | 9  |
| Table 2.2 Kerrisk's parameters.....                                 | 15 |
| Table 3.1 Description of the circuit parameters.....                | 20 |
| Table 3.2 Values of the circuit parameters of each PFU module ..... | 33 |
| Table 3.3 Specifications of the simulated EML .....                 | 35 |
| Table 3.4 Module trigger order for two scenarios .....              | 36 |
| Table 4.1 Input parameter values used in the simulation .....       | 59 |

## LIST OF FIGURES

### FIGURES

|  |    |
|--|----|
| Figure 1.1 Schematic of a sample EML system [1].                                     | 2  |
| Figure 2.1 Topology of a pulse forming unit  | 7  |
| Figure 2.2 Pulse current of a PFU  | 8  |
| Figure 2.3 Ideal current pulse   | 9  |
| Figure 2.4 Total current of 8 module connected in parallel                           | 10 |
| Figure 2.5 The separation of armature, sabot and launch object [23]                  | 11 |
| Figure 2.6 Current and magnetic field interaction (left), Lorentz force (right) [24] | 12 |
| Figure 2.7 The magnetic field produced by current passing through the rails [24]     | 13 |
| Figure 2.8 Dimensions described in Kerrisk's method                                  | 14 |
| Figure 2.9 EML system model  | 15 |
| Figure 2.10 Current path through rails and armature at low velocity [31]             | 17 |
| Figure 2.11 Current path through rails and armature at high velocity [31]            | 17 |
| Figure 3.1 EML equivalent circuit model  | 19 |
| Figure 3.2 Current path 1  | 20 |
| Figure 3.3 Current path 2  | 21 |
| Figure 3.4 Multistage EML equivalent circuit model                                   | 23 |
| Figure 3.5 Electromagnetic force and its components                                  | 26 |
| Figure 3.6 Input parameters  | 27 |
| Figure 3.7 Switch time set for each PFU  | 27 |
| Figure 3.8 Module voltage block  | 28 |
| Figure 3.9 Module current block  | 29 |
| Figure 3.10 Total current calculation block  | 29 |
| Figure 3.11 Rail, velocity skin effect, armature and contact resistances             | 30 |
| Figure 3.12 Lprime calculation block   | 30 |
| Figure 3.13 Kinematic model block  | 31 |
| Figure 3.14 Efficiency block   | 31 |
| Figure 3.15 Outputs of EML system  | 32 |
| Figure 3.16 Input section for Simpler model  | 33 |

|   |    |
|---|----|
| Figure 3.17 Circuit model for 200-kJ unit module .....  | 34 |
| Figure 3.18 Load components .....   | 34 |
| Figure 3.19 Kinematic equation blocks .....   | 35 |
| Figure 3.20 Module 1 current .....  | 37 |
| Figure 3.21 Total current passing through the rails .....   | 37 |
| Figure 3.22 Velocity of the launch object .....   | 38 |
| Figure 3.23 Position of the launch object .....   | 38 |
| Figure 3.24 Total resistance of the rails and the launch object.....  | 39 |
| Figure 3.25 Acceleration curves of the launch object .....  | 40 |
| Figure 3.26 Module 4 current .....  | 41 |
| Figure 3.27 Total current passing through the rails .....   | 41 |
| Figure 3.28 Velocity of the launch object .....   | 42 |
| Figure 3.29 Position of the launch object .....   | 42 |
| Figure 3.30 Total resistance of the rails and the launch object.....  | 43 |
| Figure 4.1 Circuit schematic of the PFU and DC voltage source.....  | 45 |
| Figure 4.2 Schematic (left ) and rotation axis (right) of the mechanism designed to represent the rails and the launch object ..... | 46 |
| Figure 4.3 Circuit schematic of the system .....  | 47 |
| Figure 4.4 Load used in the experiment .....  | 47 |
| Figure 4.5 Aluminum samples used in the experiment .....  | 48 |
| Figure 4.6 Schematic of measurements .....  | 48 |
| Figure 4.7 Basic form of Rogowski current probe [35].....   | 49 |
| Figure 4.8 DC Voltage source, oscilloscope and probes .....   | 50 |
| Figure 4.9 Pulse Forming Unit and load.....   | 50 |
| Figure 4.10 Waveforms for poorly adjusted aluminum-copper contact.....  | 51 |
| Figure 4.11 Waveforms for well-adjusted aluminum-copper contact .....   | 52 |
| Figure 4.12 Waveforms for well-adjusted aluminum-copper contact for 0.6 cm wide aluminum plate .....                                | 52 |
| Figure 4.13 Deformation in the copper rod and aluminum plates .....   | 53 |
| Figure 4.14 Resistance waveform for the time interval between 8ms and 26 ms .....   | 53 |
| Figure 4.15 Resistance waveform for the time interval between 10 ms and 24 ms .....   | 54 |
| Figure 4.16 Curve fitting waveform and actual waveform.....   | 55 |
| Figure 4.17 Input parameters for the system in Simulink .....   | 56 |
| Figure 4.18 Input parameters for the system in Simplorer .....  | 56 |
| Figure 4.19 Module voltage and module current block in Simulink .....   | 57 |

|  |    |
|--|----|
| Figure 4.20 Circuit schematic in Simplorer .....                       | 57 |
| Figure 4.21 Implementation of load resistance model in Simulink .....  | 58 |
| Figure 4.22 Implementation of load resistance model in Simplorer ..... | 58 |
| Figure 4.23 Comparison of the current curves.....                      | 59 |

## **LIST OF ABBREVIATIONS**

|       |  |
|-------|--|
| ADD   | Agency for Defense Development                     |
| DC    | Direct Current                                     |
| EMALS | Electromagnetic Aircraft Launch System             |
| EML   | Electromagnetic Launch or Electromagnetic Launcher |
| FEM   | Finite Element Method                              |
| ISL   | Institute of Saint-Louis                           |
| KERI  | Korea Electrotechnology Research Institute         |
| KVL   | Kirchhoff's Voltage Law                            |
| PFU   | Pulse Forming Unit                                 |
| PFUs  | Pulse Forming Units                                |
| PFU-1 | Pulse Forming Unit 1                               |
| VSEC  | Velocity Skin Effect                               |





## **CHAPTER 1**

### **INTRODUCTION**

#### **1.1. General Information on Electromagnetic Launchers**

The conservation of energy principle states that energy can neither be created nor destroyed; it is just transformed from one form to another. The process of changing of energy from one form to another is called energy transformation. There are many different types of energy transformations, for example an electric generator converts mechanical energy to electrical energy or a solar cell converts the radiant energy of sunlight into electrical energy, etc. One type of transformation is the conversion of electrical energy into kinetic energy, energy of motion. A classic example of this type is electric motors. Besides, a specific application of this kind of conversion is electromagnetic launchers, for which a lot of research and development studies have been done in the recent years.

Electromagnetic launcher is a device that accelerates a projectile using electrical current. It has a large power source connected to two parallel located conductive rails. A conductive material, called armature in this application, closes the circuit by acting as a shunt between two rails, by this way, current flows from one rail to another. While the current flows, it creates magnetic field according to the well-known right hand rule in such a way that magnetic field lines are perpendicular to the rails and armature. This magnetic field lines and current passing through armature produces a force, called Lorentz force, which accelerates the armature along the rails.

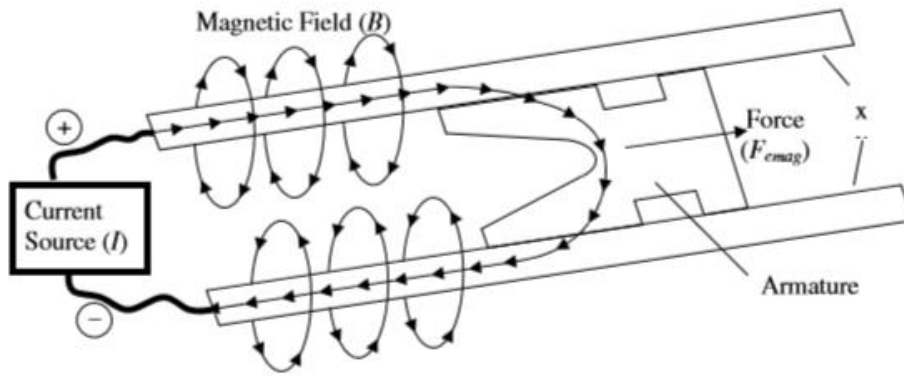


**Figure 1.1** Schematic of a sample EML system [1].

Electromagnetic launch studies mainly focus on three areas:

- i. Suborbital payload launch;
- ii. Electromagnetic aircraft launch system (EMALS);
- iii. Electromagnetic railgun.

Launching an object into space using rockets is expensive because conventional rockets need large amount of chemical fuel to use against gravity. In addition to that, the mass of the payload it launches is only around 5% of the mass of fuel it uses [2]. Therefore, alternative methods have been investigated to launch objects into space with less cost and in a more efficient way. An alternative way to launch suborbital payloads is “electromagnetic launch”. It is inexpensive because it doesn’t require heavy chemical non-reusable fuel to accelerate the projectiles and launcher can be reused many times. While a typical sounding rocket needs to carry 500 kg payload to reach the heights between 50 km to 1500 km, the mass of electromagnetic launcher projectile used for the same application is about a few kilograms [3]. The mass of projectile decreases as the use of heavy fuel decreases and hence less amount of energy is required to launch them. Experimental results have shown that projectile energy of 32MJ can be reached with energy conversion efficiency of 33%, which is more than enough for a projectile of 3.9 kg carrying 1 kg payload to reach the apogee of 120 km with a muzzle velocity of 2.1km/s [3]. However, this technology is now used for lower altitude launches that stay in space for short time to conduct scientific experiments. For stable orbit payload launches, higher projectile velocities are needed, which in

turn results in higher atmospheric friction. This friction could melt the payload or air-drag force would prevent the projectile to reach orbit altitude. New methods are needed and more research and development studies have to be done to overcome these problems [4], [5].

Electromagnetic launcher systems have also been used for launching jets and drones from an aircraft carrier. Steam catapults have been used lately for launching; however, they are large, heavy and maintenance for these systems is very hard. They also press stress on aircrafts and shorten their services. Electromagnetic launchers; on the other hand, propose to occupy lower space, decrease maintenance requirements and offer a controllable launch. Catapult systems have no feedback control, in other words, once the launch starts, the final aircraft velocity cannot be adjusted again and may be affected by many unexpected environmental factors. However, electromagnetic launchers measure aircraft speed during the launch and have a control system which ensures that the final speed of aircraft is the value decided before the launch.

Third and the last area where electromagnetic launch studies mostly concentrate on is railgun systems. Significant efforts have been made and great amount of research has been done to use them for military purposes. Railguns fire projectiles with hypervelocity which none of conventional weapons are able to reach. Thus the projectiles have longer ranges with these hypervelocity than conventional weapons. Furthermore, railgun systems are safer since they do not use explosives or fuel for launching objects. Railgun systems take less space and their cost per shot is far less when compared to gun systems which are expected to be replaced by railguns in military in the future.

## **1.2. Recent EML Research**

EML studies in different countries are given in the following parts of the thesis.

### **1.2.1. United States of America**

Railgun studies in the United States started in 1986 when “Green Farm Electric Gun Facility” was built to develop electromagnetic launcher [6]. In 1990, United States

and United Kingdom built a laboratory in Kirkcudbright, Scotland for electromagnetic launch studies. This laboratory was used actively until 2004 [7, 8]. In 2005, Office of Naval Research initiated “Electromagnetic Railgun Innovative Naval Prototype” program. The program includes two phases. Goal of Phase 1 was proof-of-concept demonstration of 32 MJ muzzle energy railgun and it was achieved in 2012. Phase 2 started in 2012 and demonstration of repetitive firing is aimed. Phase 2 is expected to be completed in 2017.

### **1.2.2. Europe**

The leading center for railgun research in Europe is the Institute of Saint-Louis (ISL), which is a French-German research institute. Railgun studies in ISL started in 1987. A lot of different scale railgun prototypes have been produced and tested [9-12] by the researchers in ISL. ISL also works with similar research groups on different topics. It collaborates with the Royal Military Academy in Belgium on augmented railguns, the University of Pisa in Italy on magnetic fields and the Institute for Semiconductor Physics in Vilnius, Lithuania on sensors.

There is also an academic paper about suborbital payload launch published by researchers from ISL [13].

### **1.2.3. China and Other Asian Countries**

China is the leading country on the number of published academic papers in the field of electromagnetic launch. The activity has greatly increased since a decade and there are lots of institutes located in China that conduct research in this area. Moreover, there are a lot of railgun prototypes countrywide [14-16].

Researchers in South Korea have been working on railgun since 2011. “Agency for Defense Development (ADD)”, “Korea Electrotechnology Research Institute (KERI)” and “Hyundai Wia Co.” collaborate in railgun studies [17-19].

There are also academic papers published by a research group at the University of Tabriz, Iran [20], [21].

### **1.3. Purpose of Thesis**

Simulations are commonly used to support experimental investigations. It is important to obtain detailed information on the behavior of the system before conducting experiments. Once the behavior is known, a model to represent the overall system can be developed. A validated simulation model is then used to predict the results of similar experiments. Moreover, the model can be used for optimization purposes.

Electromagnetic launch system includes many different parameters. Large number of experiments has to be done to investigate the impact of each parameter change on the system. However, it would be time consuming and costly. The purpose of this thesis is to develop an electromagnetic launcher model and verify it with experimental results. The model is built to include all of the variables within the system. Effect of each variable on the system may be analyzed separately.

### **1.4. Outline of Thesis**

This dissertation contains five chapters.

Chapter 1 overviews electromagnetic launch and electromagnetic launch applications. EML research studies worldwide are summarized. Importance of modeling efforts in EML studies is also underlined. In addition, the overall goal of this thesis is stated.

Chapter 2 elaborates electromagnetic launcher components. Using electromagnetic launch theory, Lorentz equation, known as the basis of electromagnetic launch, is evaluated and simplified to the well-known formula. Moreover, different approaches used in modeling studies are presented.

Chapter 3 details electrical and kinematic models of an EML. All of the equations related with these models are derived. Two different models are developed based on these equations. A new approach is proposed for Simulink model. The proposal, which offers defining two different current paths instead of one as in [20], [22] while writing the current equation, may provide more realistic results. An EML system is simulated using two models and results are compared.

Chapter 4 includes the validation of the models through experiments. Experimental goals and components are stated. Measurement methods are elaborated. In addition, experimental results are analyzed to obtain a model to use in simulations. The models are updated to represent the system used in the experiment. In the end, simulation results and experimental results are compared and discussed.

Finally, the dissertation concludes with a summary of the work done. Information and experience gained through the study is presented. Future work is also proposed.

## CHAPTER 2

### EML BACKGROUND

#### 2.1. Structure of EML

Electromagnetic launcher consists of three main parts:

- i. Pulse Forming Unit (PFU);
- ii. Conductive rails;
- iii. Launch objective.

##### 2.1.1. Pulse Forming Unit

PFU creates a current pulse that accelerates the projectile through the rails. PFU includes a pulsed power source, a high voltage switch, a crowbar diode, a pulse shaping inductor and power cables that provide connection to the rails. Topology of a PFU circuit is shown in Figure 2.1.

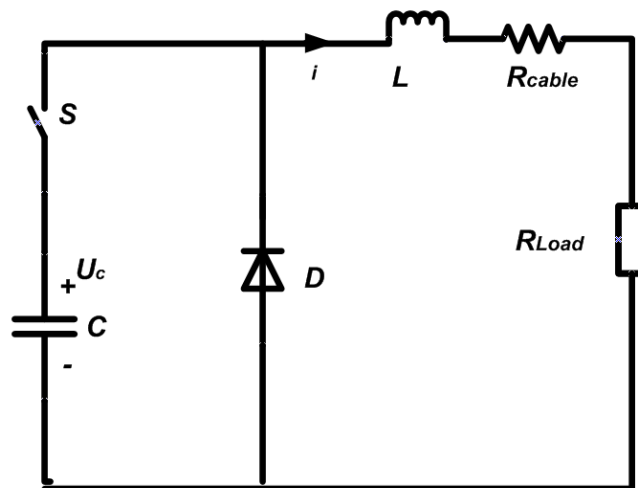


**Figure 2.1** Topology of a pulse forming unit

In EML applications, various different numbers of capacitors are charged with DC current. The number of capacitors required scales by energy rating of the application. Charged capacitors discharge over an inductor. Inductor is used to adjust peak current and discharge duration, in other words, controls the shape of the pulse current. Discharge start time is controlled by using high voltage switches. Generally, thyristors and spark gaps are selected for this process. Pulse current is finally transferred to rails by power cables. Simulation result for a pulse current of a PFU which has 4 mF, 10 kV capacitor and 10  $\mu$ H inductor is shown in Figure 2.2. Discharge start time is set to  $t = 0$ .

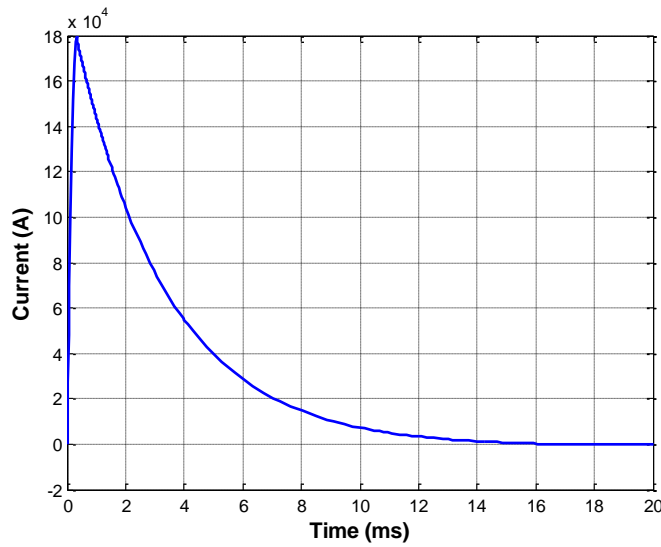


**Figure 2.2** Pulse current of a PFU

The major purpose of pulse forming unit studies is to have a current pulse close to a rectangular shape, which is accepted as the ideal current pulse. In ideal current pulse case, which is shown in Figure 2.3, current reaches instantly to a value of  $I_0$  and maintains its value until projectile leaves the rails. As the projectile exits the rails, the current should then drop to zero.  $I$  and  $t$  represents current and time.



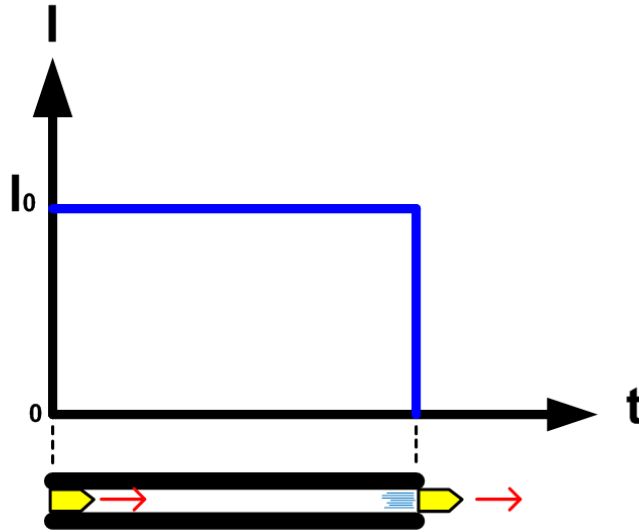


**Figure 2.3** Ideal current pulse

It is not practical to start and stop current flow instantaneously since all systems have internal inductance; therefore, ideal current pulse remains a theory. However, a current pulse can be approximated to the ideal current pulse by using more than one PFU. Several PFUs connected to the same rails with different and appropriate discharge start time provide flat current pulses. Simulation result for total current of 8 modules connected in parallel is given in Figure 2.4. Modules are identical and each has 4 mF, 10 kV capacitor and 10  $\mu$ H inductor. Discharge start time for each module is given in Table 2.1.

**Table 2.1** Discharge start time for each module

| Module number | Discharge start time (ms) |
|---------------|---------------------------|
| 1             | 0                         |
| 2             | 0                         |
| 3             | 0                         |
| 4             | 0.8                       |
| 5             | 2                         |
| 6             | 3                         |
| 7             | 4.2                       |
| 8             | 5.4                       |

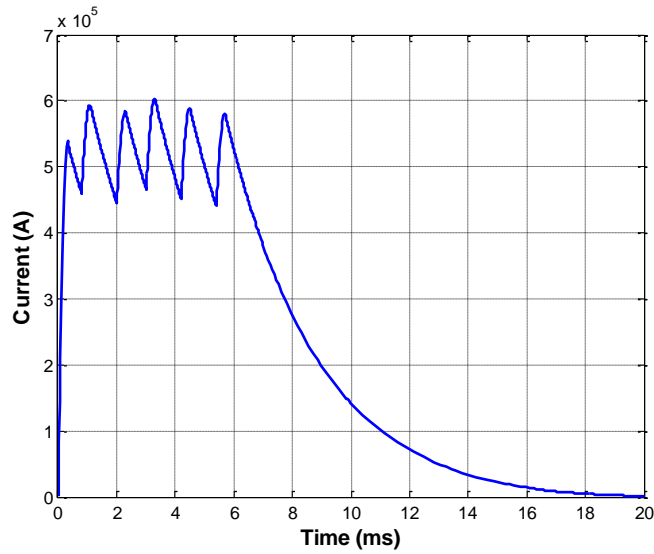


**Figure 2.4** Total current of 8 module connected in parallel

### 2.1.2. Conductive Rails

Rail pair is used as barrel in EML. Projectile is placed between parallel rails. When the current pulse produced by PFU flows through rails and armature, armature starts sliding along the rails. Current pulse peak value is generally in the order of several hundred kA; therefore, a significant amount of initially charged electrical energy is lost due to rail resistance in the form of heat dissipation. Furthermore, the contact between projectile and rails causes friction force that also decelerates the projectile. Hence, it can be said that rail material plays an important role in the efficiency of launch application. Materials that have high electrical conductivity and small friction coefficient should be used as rails. Also, roughness of the surface of the rails should be as good as possible so that the contact resistance between projectile and rails can be kept low.

### 2.1.3. Launch Object

Launch object generally consists of three parts. First part is the conductive part which is called armature. Second part is a non-conductive part called sabot. It is used to hold projectile in a precise position. Third part includes the object that is aimed to launch and it is called projectile. Armature holds the projectile and sabot while conducting current between the rails. As current passes through the armature, armature, sabot and

projectile starts moving with the effect of electromagnetic force acting on the armature. After they leave the barrel, armature drops first. Then sabot are separated from projectile by air drag force. Sabot falls away and projectile flies with hypervelocity. An example of sabot separation is illustrated in Figure 2.5.

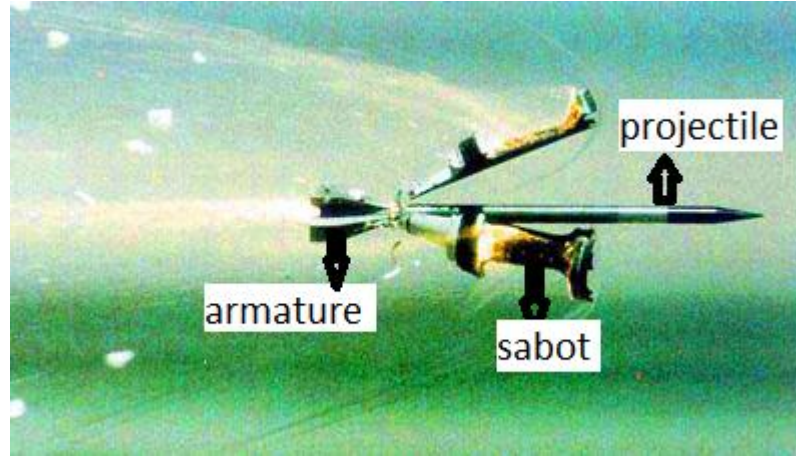


**Figure 2.5** The separation of armature, sabot and launch object [23]

## 2.2. Electromagnetic Launch Theory

The principle of electromagnetic launch technology relies on the Lorentz force, which describes the interaction between electrical current and magnetic fields. This force is defined by

$$\vec{F} = q(\vec{v}_d \times \vec{B}) \quad (2.1)$$

As armature completes the circuit path between the rails, current passes through rails and armature with a drift velocity ( $\vec{v}_d$ ). The current flowing through the rails also creates a magnetic field ( $\vec{B}$ ) between the rails. These perpendicular velocity and magnetic field vectors result in a force ( $\vec{F}$ ) on any charged particles ( $q$ ) between the rails. Figure 2.6 illustrates this interaction.

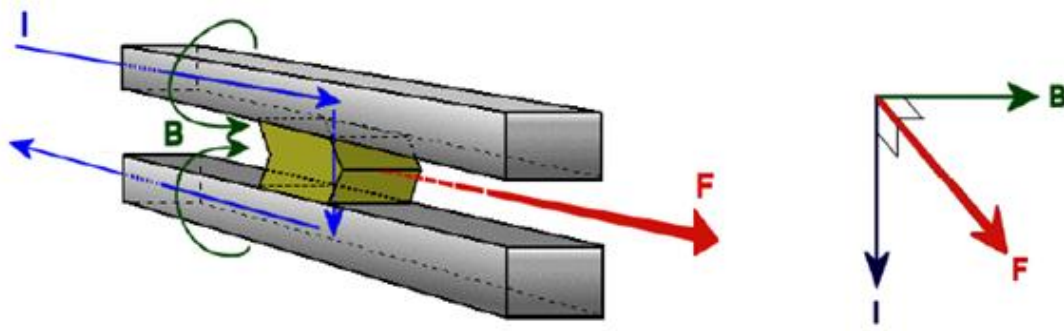


**Figure 2.6** Current and magnetic field interaction (left), Lorentz force (right) [24]

To better understand the interaction between the projectile and rails, the magnitude of the Lorentz force can be given as

$$F = qv_d B \quad (2.2)$$

where  $q$  is charge,  $v_d$  is the magnitude of the drift velocity of the charge, and  $B$  is the magnitude of the magnetic field created between the rails. The amount of charge flowing through the projectile can be written as

$$q = It \quad (2.3)$$

where  $I$  is the current and  $t$  is the passing time of a charge with a velocity of  $v_d$  through the projectile having a length of  $l$ . Equation 2.3 can be rewritten as

$$q = I \frac{l}{v_d} \quad (2.4)$$

Replacing  $q$  in Equation 2.2 using Equation 2.4 gives the resulting equation

$$F = BIl \quad (2.5)$$

Differentiating Equation 2.5 along the armature height  $l$  yields the following

$$dF = Bldx \quad (2.6)$$

Equation 2.6 shows a relationship between Lorentz force acting on the armature, magnetic field and the electrical current. The magnetic field  $B$  produced by a current passing through a semi-infinite straight wire can be expressed by Biot-Savart Law as

$$B = \frac{\mu_0 I}{4\pi r} \quad (2.7)$$

where  $\mu_0$  is permeability of free space and  $r$  is the radial distance from the center of wire. Now, two assumptions have to be made:

- i. the current passes only through the center of the rails, and
- ii. the magnetic characteristics of rectangular rails are similar to the characteristics of long circular wires.

The assumptions stated above are illustrated in Figure 2.7 below.

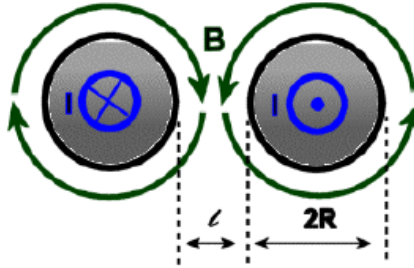


**Figure 2.7** The magnetic field produced by current passing through the rails [24]

After applying the Biot-Savart Law equation into Equation 2.6 and integrating it, Lorentz force becomes

$$F = \frac{\mu_0 I^2}{4\pi} \int_R^{R+l} \left( \frac{1}{x} + \frac{1}{2R+l-x} \right) dx \quad (2.8)$$

Evaluating the integral yields

$$F = \frac{\mu_0 I^2}{4\pi} \ln \left\{ \frac{(R+l)^2}{R^2} \right\} \quad (2.9)$$

The right hand side of the Equation 2.9 can be divided into two parts. First part is  $I^2$  and second part includes the rest. A new term is introduced in electromagnetic launch studies to define the second part. It is called inductance gradient ( $L'$ ) and it is a

magnetic field factor which depends only the geometry of the electromagnetic launcher itself. It is important to note that  $L'$  is not an inductance of the system and its unit is  $H/m$ . Therefore,  $L'$  is expressed as

$$L' \equiv \frac{\mu_0}{2\pi} \ln \left\{ \frac{(R+l)^2}{R^2} \right\} \quad (2.10)$$

Finally, substituting Equation 2.10 into 2.9 gives the simple Lorentz Force equation

$$F = \frac{1}{2} L' I^2 \quad (2.11)$$

### 2.3. Inductance Gradient

Inductance gradient is one of the important parameters to determine the Lorentz force; therefore, it has to be calculated accurately. Kerrisk's method is widely used to find  $L'$  of the EML systems [25].

The method developed at Los Alamos National Laboratory includes the geometry of the rails and various material and logarithmic constants.

$$L' = \left[ A + B \ln \left( a_1 \frac{w}{h} + a_2 \frac{w}{h} \frac{s}{h} \right) \right] \ln \left( b_1 + b_2 \frac{s}{h} + b_3 \frac{s}{h} + b_4 \frac{s}{h} \frac{w}{h} \right) \quad (2.12)$$

where  $w$  is rail width,  $s$  is rail separation and  $h$  is rail height as shown in Figure 2.8. Kerrisk's parameters are given in Table 2.2.

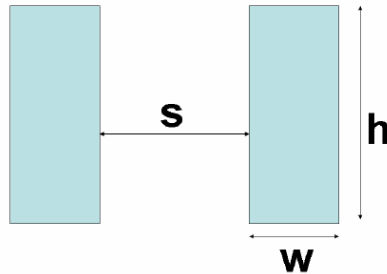


**Figure 2.8** Dimensions described in Kerrisk's method

**Table 2.2** Kerrisk's parameters

| <b>Kerrisk's parameters</b> |          |
|-----------------------------|----------|
| $A$                         | 0.44061  |
| $B$                         | -0.0771  |
| $a_1$                       | 3.397143 |
| $a_2$                       | -0.06603 |
| $b_1$                       | 1.007719 |
| $b_2$                       | 2.743651 |
| $b_3$                       | 0.022093 |
| $b_4$                       | 0.263739 |

#### 2.4. Literature Review

Global electromagnetic launcher model can be constructed by combining electrical model of the pulse forming network, the rails and the armature with kinematic model of the armature.

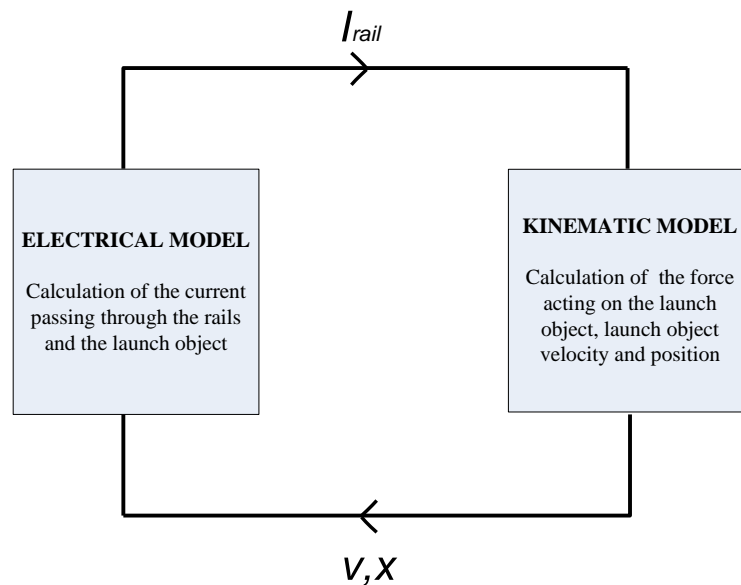


**Figure 2.9** EML system model

Electrical model is used to calculate the current passing through the rails. The current found in the electrical model is then used in kinematic model to find the electromagnetic force acting on the armature. The net force on the armature is obtained

by subtracting total friction force from electromagnetic force. Armature acceleration, velocity and position is calculated by making use of this net force. The rail resistance and inductance are time dependent due to moving armature along the rails. Therefore, armature velocity and position found in the kinematic model are then used in the electrical model to calculate the rail current.

The efforts on modeling and simulation of EML system are based on solving nonlinear differential equations coming from the electrical and kinematic models. Different ways to express these equations were published in the past. Since the armature is driven by electric current, it is a natural approach to use electrical circuit simulation environments. M. Coffo and J.Gallant [26] used PSPICE to model the system by converting all constitutive equations into circuits consisting of basic circuit elements. Y. Zhou *et al.* [27] also used PSPICE to build the models and do the analysis and verified the model with experimental results. F.J. Deadrick *et al.* [28] expressed the equations as a software program and used solver libraries.

Another approach to simulate the system is to use block diagram model for differential equation system of the pulsed power supply and the launcher. T.Sianen *et al.* [22] used SCILAB to present a simulation model. S.A.Taher *et al.* [20] used Simulink for block diagram model and validated its accuracy with experimental and finite element method (FEM) results. Yu and Fan [29] have attempted to use Simulink and Simplorer to analyze the EML system, where electrical circuit simulation results obtained in Simplorer are used to solve kinematic equations modeled in Simulink. Monte Carlo method was also implemented to simulate EML [30].

As mentioned above, the rail resistance changes with time as armature moves through the rails. Therefore, a time dependent model is needed to represent the resistance of the rails. In related references, T.Sianen *et al.* [22] used a linear model, which follows

$$R_{\text{var}}(t) = R'x(t) + R_0 \quad (2.13)$$

where  $x(t)$  is the position of the armature,  $R'$  is the resistance per unit length and  $R_0$  is the initial resistance. This assumption ignores the current skin effect and the contact resistance when establishing the rail resistance. When the velocity of the armature is



low, the current could flow uniformly between the conductors, which is shown in Figure 2.10.

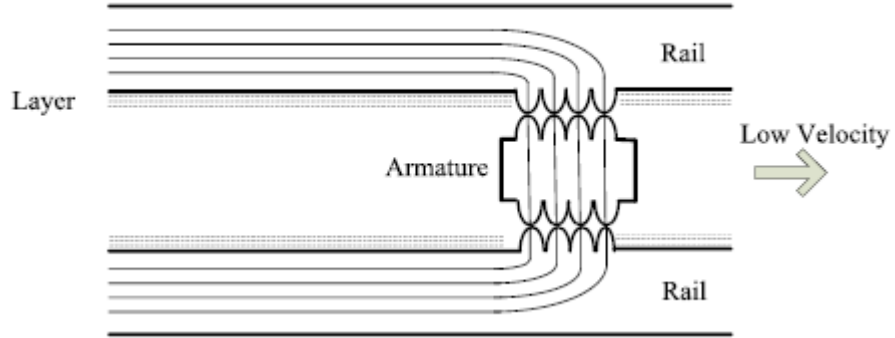


**Figure 2.10** Current path through rails and armature at low velocity [31]

However, when the velocity is high, the density of the current through the rails and armature changes in a way that current flows through the trailing edge of the armature as shown in Figure 2.11.

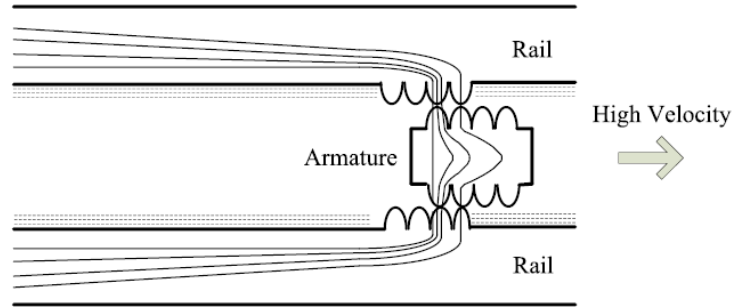


**Figure 2.11** Current path through rails and armature at high velocity [31]

Rail resistance, Velocity Skin Effect (VSEC) resistance and contact resistance are all formulated by taking the skin effect into consideration. The total rail resistance is modeled in [27], [32], [33] as

$$R_{total} = R_{rail} + R_{VSE} + R_S + R_C \quad (2.14)$$

where  $R_{rail}$  is the resistance of the rails,  $R_{vSEC}$  is the change of contact resistance caused by speed skin effect,  $R_s$  is the resistance of the armature and  $R_c$  is the contact resistance.

J.Wey *et al.* [34] also used a model regarding the skin effect. In that model an equivalent resistance equation for rails is given as

$$R_{rail}(t) = R'(t)x(t) \quad (2.15)$$

$$R'(t) = R_0 \left[ \sqrt{\frac{t_0}{t}} + erf\left(\sqrt{\frac{t_0}{t}}\right) \right] \quad (2.16)$$

where  $R'_0$  is the variation due to normal skin depth and  $t_0$  is a typical time constant in the order of 1 ms. M. Coffo and J.Gallant [26] also used this representation for rail resistance in their EML model.

## CHAPTER 3

### EML MODELING

#### 3.1. Electrical Model

##### 3.1.1. Basic Form of EML

Mathematical equations are used to represent a system in Simulink. These equations are then solved by an appropriate solver chosen in the program. Therefore, all mathematical equations related to EML system have to be derived first.

Equivalent circuit model of the launcher can be drawn as in Figure 3.1. Description of the circuit parameters is given in Table 3.1.

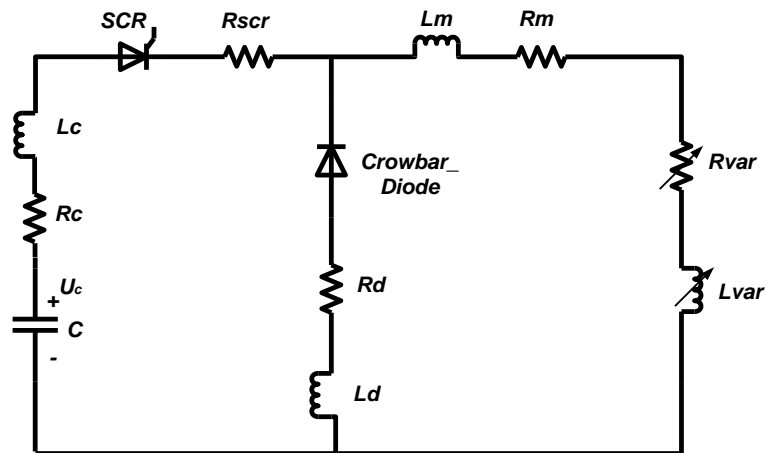
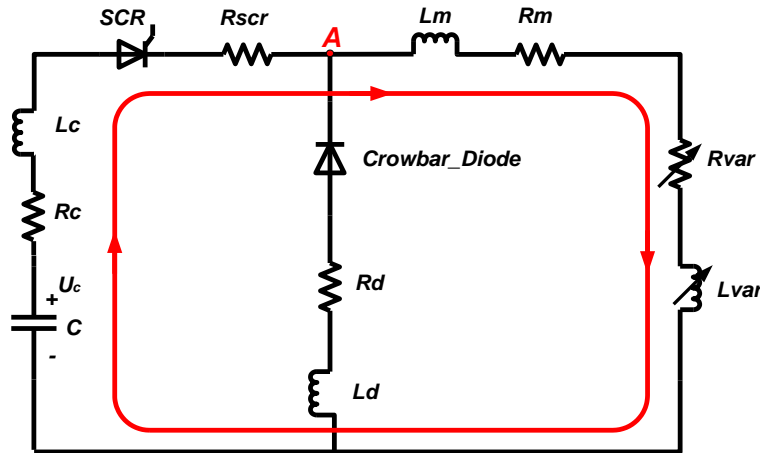


Figure 3.1 EML equivalent circuit model

**Table 3.1** Description of the circuit parameters

| Parameter | Description   |
|-----------|---|
| $R_c$     | Equivalent series resistance of capacitor                               |
| $L_c$     | Equivalent series inductance of capacitor                               |
| $R_{scr}$ | Resistance of silicon controlled rectifier stack                        |
| $R_d$     | Resistance of crowbar diode stack                                       |
| $L_d$     | Inductance of crowbar diode stack                                       |
| $R_m$     | Total resistance of pulse shaping inductor and power cables in a module |
| $L_m$     | Total inductance of pulse shaping inductor and power cables in a module |
| $R_{var}$ | Total resistance of rails and launch object                             |
| $L_{var}$ | Total inductance of rails and launch object                             |
| $U_c$     | Initial capacitor charge voltage  |

Electrical circuit equation of the system is found using Kirchhoff's Voltage Law (KVL). The current in the circuit flows through two different paths due to the existence of the crowbar diode. Current follows the path drawn in Figure 3.2 until the voltage at node A decreases to zero.

**Figure 3.2** Current path 1

Voltage equation for path 1 can be written as

$$-U_c + i(t)R_c + L_c \frac{d}{dt}i(t) + i(t)R_{scr} + i(t)R_m + L_m \frac{d}{dt}i(t) + i(t)R_{var}(t) + \frac{d}{dt}(i(t)L_{var}(t)) = 0 \quad (3.1)$$

Voltage at node A is

$$V_A = U_C - i(t)R_C - L_C \frac{d}{dt}i(t) - i(t)R_{scr} \quad (3.2)$$

Internal resistances and inductances are included in the equivalent circuit model in Figure 3.1. Their effects on the overall performance of the system should not be neglected since the current in the circuit would be at a level of a few hundred kilo amps to million amps.

The path for the current as the voltage at node A decreases to zero and the crowbar diode is in the conduction state is drawn in Figure 3.3.

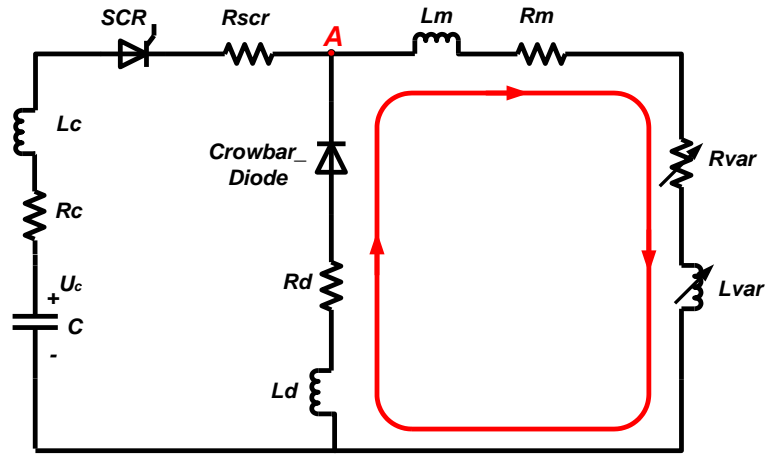


**Figure 3.3** Current path 2

Voltage equation for the second path is written as

$$i(t)R_m + L_m \frac{d}{dt}i(t) + i(t)R_{var}(t) + \frac{d}{dt}(i(t)L_{var}(t)) + i(t)R_d + L_d \frac{d}{dt}i(t) = 0 \quad (3.3)$$

It should be noted that the initial value of the current  $i(t)$  in Equation 3.3 is the final value of the current found in the solution of Equation 3.1, which corresponds to the peak value of the total current in the module. The variable resistance of the launcher  $R_{var}$  and the variable inductance  $L_{var}$  both depend on the position of the launch object. The relationship for the resistance will be detailed in the following sections; however,

$L_{\text{var}}$  has to be analyzed at this stage due to the presence of  $\frac{d}{dt}(i(t)L_{\text{var}}(t))$  term in both Equation 3.1 and Equation 3.3. The inductance of the rails is assumed to have a linear relationship with the position of the launch object. It follows

$$L_{\text{var}}(t) = L' x(t) \quad (3.4)$$

where  $L'$  is the inductance per unit length, i.e. inductance gradient and  $x(t)$  is the position of the launch object. Equation 3.1 and Equation 3.3 may be rewritten as

$$\begin{aligned} -U_c + i(t)R_c + L_c \frac{d}{dt} i(t) + i(t)R_{scr} + i(t)R_m + L_m \frac{d}{dt} i(t) + i(t)R_{\text{var}}(t) + L' x(t) \frac{d}{dt} i(t) \\ + i(t) \frac{d}{dt} L' v(t) = 0 \end{aligned} \quad (3.5)$$

$$i(t)R_m + L_m \frac{d}{dt} i(t) + i(t)R_{\text{var}}(t) + L' x(t) \frac{d}{dt} i(t) + i(t) \frac{d}{dt} L' v(t) + i(t)R_d + L_d \frac{d}{dt} i(t) = 0 \quad (3.6)$$

where  $v(t)$  is the velocity of the launch object, obtained from  $\frac{d}{dt} x(t)$ .

$L' x(t)$  expresses the inductance of the rails, but  $L' v(t)$  does not have a meaning related to the inductance. According to Faraday's Law of induction,  $L' v(t)I(t)$  is called the back EMF and  $L' v(t)$  is a resistance that represents the mechanical energy converted from electrical energy by a magnetic field.

### 3.1.2. Multistage EML

In EML applications, a multistage structure is used instead of a single PFU to eliminate the limitations and improve the performance of the system. The current passing through each electronic component in a PFU, which is the main concern in designing of a PFU, decreases as several numbers of PFUs are connected in parallel. Moreover, increasing number of PFUs gives the advantage to shape the rail current by triggering each PFU in an order to increase the acceleration of the launch object.

Equivalent circuit model for the multistage EML is given in Figure 3.4.

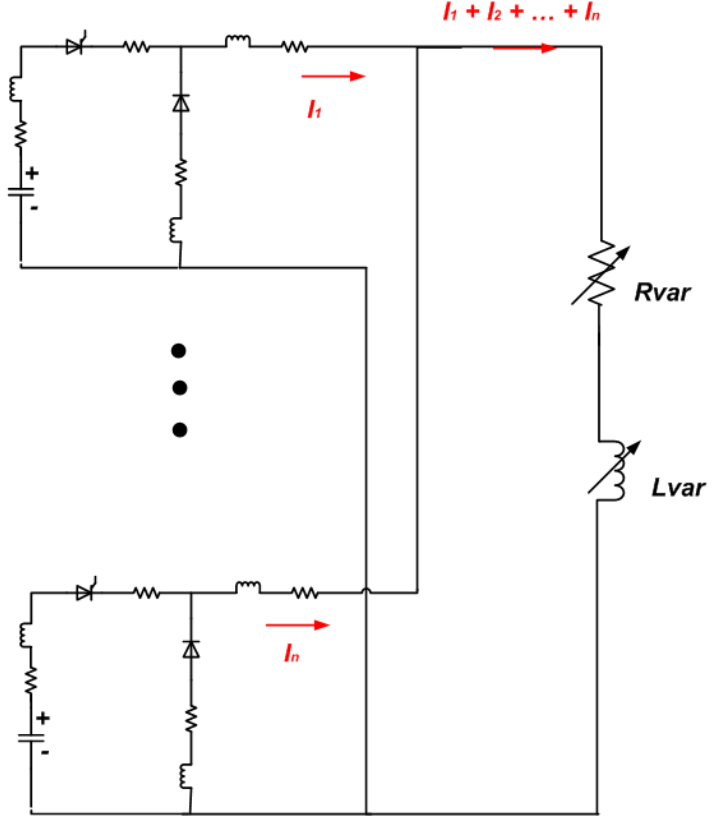


**Figure 3.4** Multistage EML equivalent circuit model

Modifying Equation 3.5 and Equation 3.6 for multistage EML model yields

$$\begin{aligned}
 & -U_c + i_1(t)R_c + L_c \frac{d}{dt} i_1(t) + i_1(t)R_{scr} + i_1(t)R_m + L_m \frac{d}{dt} i_1(t) + i_{total}(t)R_{var}(t) + \\
 & L' x(t) \frac{d}{dt} i_{total}(t) + i_{total}(t) \frac{d}{dt} L' v(t) = 0
 \end{aligned}
 \tag{3.7}$$

$$\begin{aligned}
 & i_1(t)R_m + L_m \frac{d}{dt} i_1(t) + i_{total}(t)R_{var}(t) + L' x(t) \frac{d}{dt} i_{total} + i_{total}(t) \frac{d}{dt} L' v(t) + \\
 & i_1(t)R_d + L_d \frac{d}{dt} i_1(t) = 0
 \end{aligned}
 \tag{3.8}$$

where  $i_1(t)$  is the current in PFU-1 and  $i_{total}(t)$  is the sum of the currents in each PFU.

$$i_{total}(t) = i_1(t) + i_2(t) + \dots + i_n(t) \quad (3.9)$$

The variable rail resistance is modeled as in [29]. In this model, velocity skin effect due to sliding contact, current skin effect and imperfect contact effect are all taken into consideration and each is represented as a part of total rail resistance. Resistance equations for the rails, the launch object, the contact between rails and launch object and velocity skin effect are defined as

$$R_g(x) = \begin{cases} \frac{8x}{3h} \sqrt{\frac{\pi\mu\rho}{2t}}, & x \leq l \\ \frac{8l}{3h} \sqrt{\frac{\pi\mu\rho}{2t}}, & x > l \end{cases} \quad (3.10)$$

$$R_s = \frac{s}{h} \sqrt{\frac{\pi\mu\rho}{2t}} \quad (3.11)$$

$$R_c = \frac{k_c}{h} \sqrt{\frac{\pi\mu\rho}{2t}} \quad (3.12)$$

$$R_{vsec}(v) = R_{vc} * \sqrt{v^3} \quad (3.13)$$

where  $R_g(x)$  is the rail resistance,  $R_s$  is the resistance of the launch object,  $R_c$  is the contact resistance and  $R_{vsec}(v)$  is the resistance due to velocity skin effect.  $l$  is the length of the rails,  $s$  is width of the launch object,  $h$  is the height of the rails.  $k_c$  is the contact resistance constant,  $\mu$  is the permeability of the rail material,  $\rho$  is the effective resistivity and  $t$  represents the time. Finally,  $R_{vc}$  is the proportionality constant and  $v$  is the velocity of the launch object.

### 3.2. Kinematic Model

Kinematic model equations arise from the classical equation



$$F_{net} = ma \quad (3.14)$$

where  $F_{net}$  is the net force acting on the launch object,  $m$  is the mass of the launch object and  $a$  is the acceleration of the launch object. The net force on the launch object is found by subtracting the mechanical friction force  $F_f(t)$  from the electromagnetic force  $F_{em}(t)$ , assuming that all other forces acting on the launch object are negligible.

$$F_{net} = F_{em} - F_f \quad (3.15)$$

The electromagnetic force  $F_{em}(t)$  is simply found by using Lorentz force equation,

$$F_{em} = \frac{1}{2} L' i_{total}^2 \quad (3.16)$$

The mechanical friction force is a function of the friction coefficient  $\mu_{fr}$  and the normal force  $F_N$ ,

$$F_f = \mu_{fr} F_N \quad (3.17)$$

The normal force has both mechanical ( $F_{N,mech}$ ) and electromagnetic ( $F_{N,em}$ ) components, which can be written as

$$F_N = F_{N,mech} + F_{N,em} \quad (3.18)$$

The mechanical normal force is obtained from the compression test of the launch object. However, the electromagnetic normal force is proportional to the electromagnetic force,

$$F_{N,em} = \alpha F_{em} \quad (3.19)$$

where  $\alpha$  is a proportionality constant depends on the geometry of the current bridge. The electromagnetic force and its components are shown in Figure 3.5.

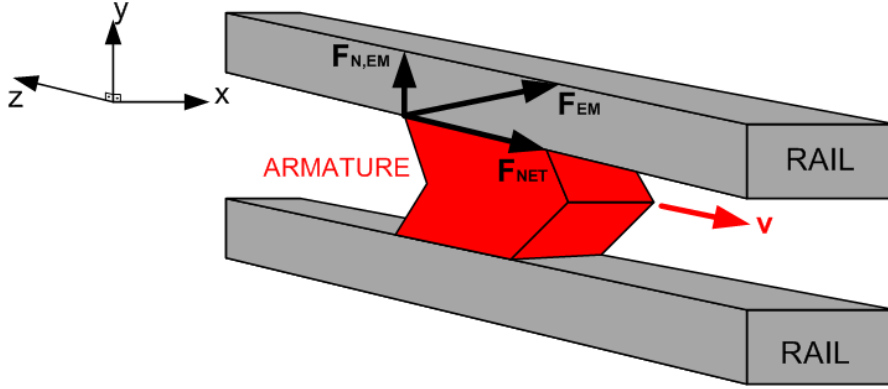


**Figure 3.5** Electromagnetic force and its components

An expression for the net force acting on the projectile is found by combining all the equations from Equation 3.14 to Equation 3.19.

$$F_{net} = F_{em} - F_f = (1 - \alpha\mu_{fr})F_{em} - \mu_{fr}F_{N,mech} \quad (3.20)$$

As the acceleration of the launch object is calculated from Equation 3.14, velocity and position of the launch object can be easily found as follows

$$v(t) = \int a(t)dt + v_0 \quad (3.21)$$

$$x(t) = \int v(t)dt + x_0 \quad (3.22)$$

### 3.3. Implementation in Simulink

All mathematical equations representing both electrical and kinematic models are expressed as block diagrams in Simulink. Each block has inputs and outputs and outputs of some blocks are used as inputs for other blocks. These relations and all the sub blocks are explained in detail in this section.

The model uses some inputs defined by the user. Input parameters are set according to the system to be modeled. These parameters include capacitor voltage, capacitance

value of PFU and all the resistances and inductances of PFU. Moreover, values of some constants such as electrical resistivity, proportionality constant and contact resistance constant are written here. Finally, the rail and the launch object dimensions and the mass of the launch object are all set in this part. Dimensions of the rails and the launch object are used to find the inductance gradient according to Equation 2.12. The mass of the launch object is used to solve the kinematic model equations.

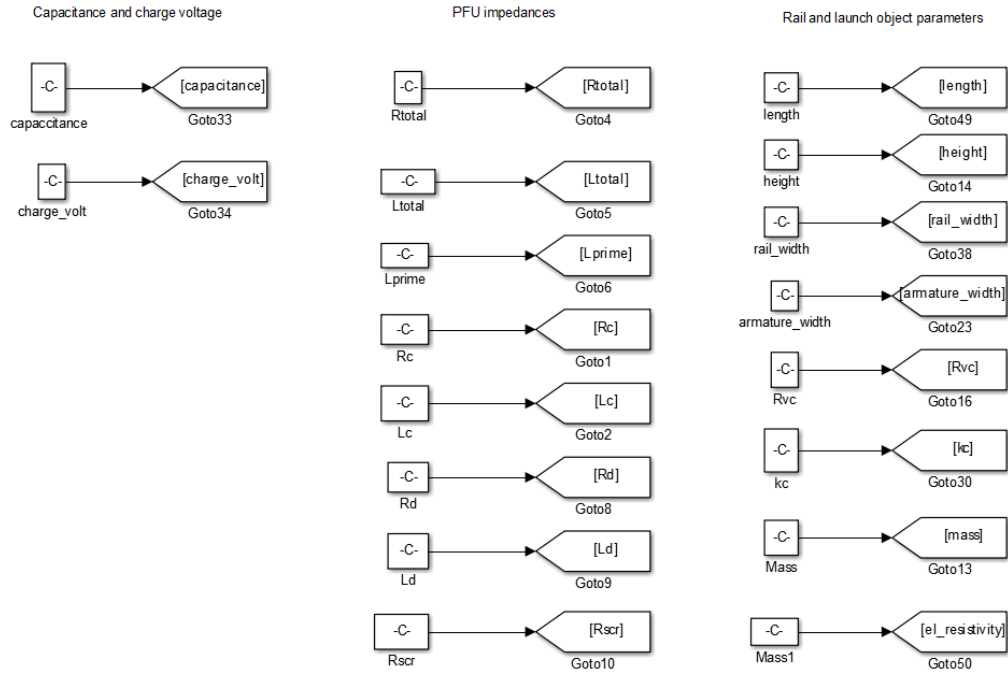


**Figure 3.6** Input parameters

Switch time of each PFU used in the system is also set by the user, as the system is multistage and each PFU is triggered independently.

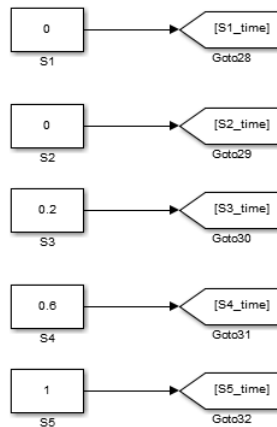


**Figure 3.7** Switch time set for each PFU

The current and the voltage of each PFU are calculated separately and then the total current is found by the summation of all module currents. A modular model approach is used so as to modify the model easily for new systems. Only by adding or removing voltage and current sub-blocks without changing other blocks, a model for the system having different number of PFUs can be modeled.

The block to find the capacitor and the diode voltage is given in Figure 3.8. This block is used to represent the Equation 3.2.

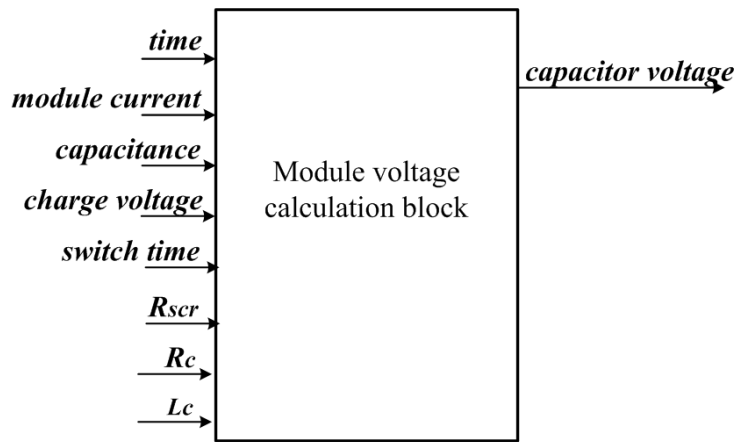


**Figure 3.8** Module voltage block

“Time” input is used as reference for switch time of each PFU. “Module\_curr” input is derived from the module current block. Capacitor inductance, resistance and thyristor resistance are also used as inputs since they exist in the equation of capacitor and diode voltage. The diode voltage found in this block is used as an input to the module current block. The module current block is shown in Figure 3.9. In this block, the diode voltage is the control input. Initially, the diode voltage is equal to the charge voltage and greater than zero; therefore, Equation 3.7 is used to find the module current. The capacitor voltage and the diode voltage decreases as the capacitor discharges over pulse shaping inductor. Equation 3.7 is valid until the diode voltage decreases to zero, after than the block representing Equation 3.8 is used for deriving the module current. It should be noted that the current used in Equation 3.8 has an

initial value. The final value of the current calculated in Equation 3.7 has to be used as the initial value for the current given in Equation 3.8.

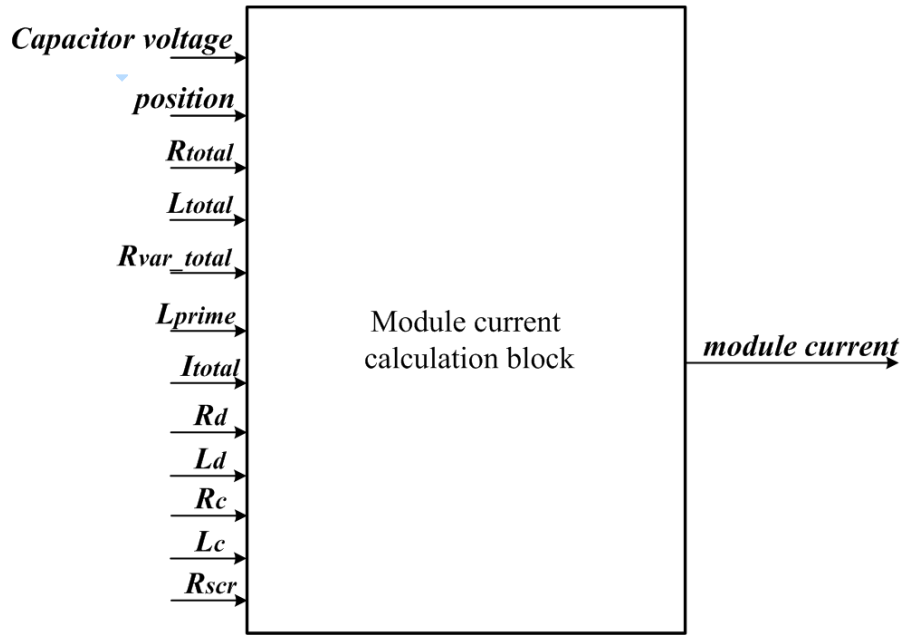


**Figure 3.9** Module current block

Unlike the approach used both in [20] and [22] to represent the EML in block diagram model, this model takes the effect of the diode resistance and inductance into account while building the model of the system. Therefore, the effect of the change in the impedance of the diode on the current waveform may be observed. This approach provides a more detailed analysis and reliable results.

As the current of each module is found, the total current is calculated by summation of the module currents.

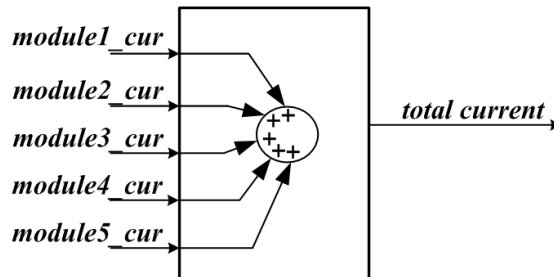


**Figure 3.10** Total current calculation block

“Rvar\_total” input of the module current block is the summation of the resistances given by the equations from Equation 3.10 to Equation 3.14. The blocks used for representing these resistances are given in Figure 3.11.

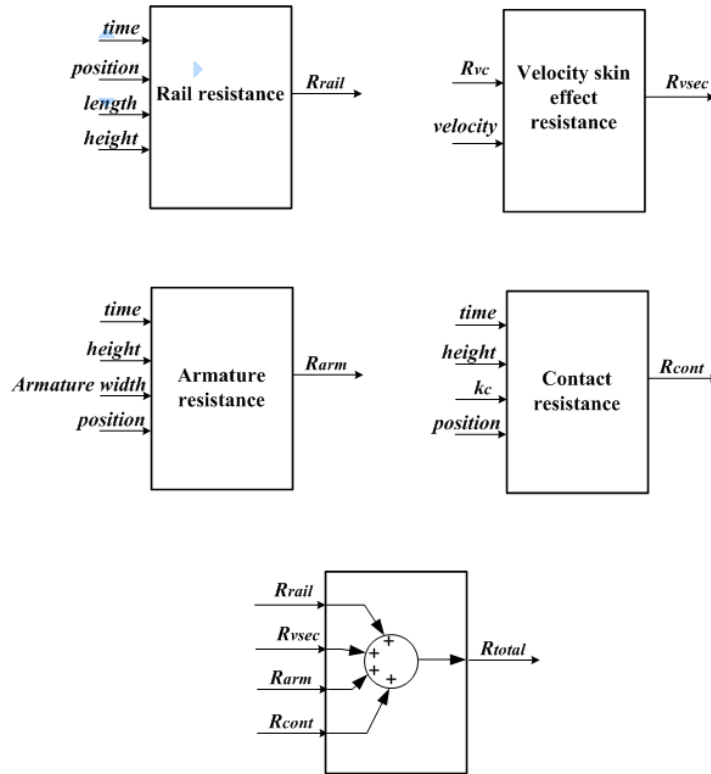


**Figure 3.11** Rail, velocity skin effect, armature and contact resistances

“Lprime” input of module current block is also found using the block built for Equation 2.12.

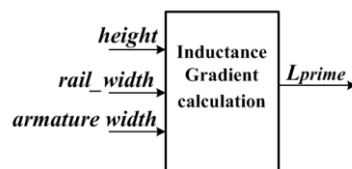


**Figure 3.12** Lprime calculation block

Kinematic equations are also expressed in the model. The block to find the acceleration, the velocity and the position of the launch object is shown in Figure 3.13.

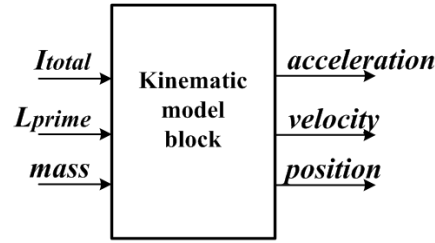


**Figure 3.13** Kinematic model block

Total current passing through the rails, inductance gradient and the mass of the launch object are inputs of the block. The acceleration of the launch object is first calculated using equations from Equation 3.14 to Equation 3.20. The velocity and the position are then found by solving Equation 3.21 and Equation 3.22.

Efficiency of the system is also figured out using the block given in Figure 3.14.

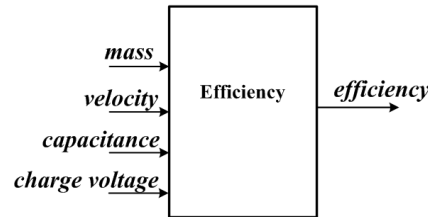


**Figure 3.14** Efficiency block

In this block, efficiency is defined as the ratio of the kinetic energy of the launch object to the charge energy of all capacitors in the system.

$$\eta = \frac{\frac{1}{2}mv^2}{\frac{1}{2}CV^2} \quad (3.23)$$

where  $m$  is mass and  $v$  is velocity of the launch object,  $C$  is total capacitance of PFU and  $V$  is charge voltage of the capacitors in the PFU.

Finally, there is an output section in the model; all the waveforms of the outputs of the system can be monitored here. Outputs to be monitored are given in Figure 3.15.

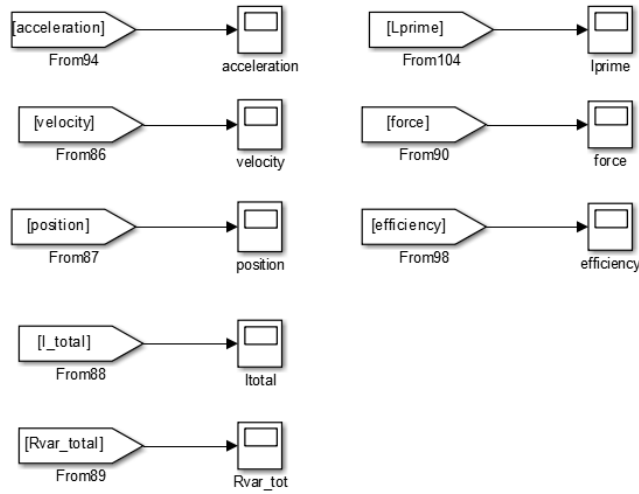


**Figure 3.15** Outputs of EML system

### 3.4. Implementation in Simplorer

Electrical components are represented numerically in Simulink. Their impedance values are used in the equations to build blocks; however, electrical circuit simulation programs serve component models in detail. For each model, all of the parameters affecting their operation are included and can be controlled by the user. Therefore, the system is also modeled in Simplorer simulation program. Simplorer is convenient in modeling electrical part of the system. Simulink; on the other hand, is suitable for representing the kinematic part. Moreover, optimization studies have to be done to increase performance of the system. Optimum switching time of each module, optimum length of the rails, etc. can all be found by analyses conducted in Simulink. It would be better to model the system in these two different simulation environments to be able to analyze the system in different aspects.

Simplorer includes library of models for electrical components. Therefore, it is easy to implement a circuit model by just choosing the component from the library, dragging it into the model and making wire connections. However, EML system includes lots of variables and effect of change in each variable may be wanted to be observed. On the other hand, since EML system consists of modules, it would be time



consuming to change a variable in all modules manually. Therefore, as in Simulink model, an input control section is built as shown in Figure 3.16. Constant values are assigned to all of the parameters and also for the switch time for each module as given in Figure 3.16. Furthermore, variables used in kinematic equation are also defined and controlled in this section.

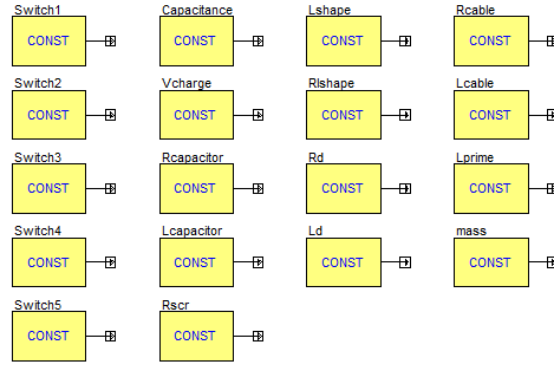


**Figure 3.16** Input section for Simpler model

The system to be modeled has 1MJ PFU. The PFU is composed of five 200-kJ unit modules. Values of circuit parameters of each module are given in Table 3.2.

**Table 3.2** Values of the circuit parameters of each PFU module

| Parameter    | Description                                      | Value           |
|--------------|--|-----------------|
| $U_c$        | Initial capacitor charge voltage                 | 10 kV           |
| $C$          | Capacitance of capacitor                         | 4 mF            |
| $R_c$        | Equivalent series resistance of capacitor        | 0.25 m $\Omega$ |
| $L_c$        | Equivalent series inductance of capacitor        | 0.1 $\mu$ H     |
| $R_{scr}$    | Resistance of Silicon Controlled Rectifier Stack | 1 m $\Omega$    |
| $R_d$        | Resistance of crowbar diode stack                | 0.6 m $\Omega$  |
| $L_d$        | Inductance of crowbar diode stack                | 0.1 $\mu$ H     |
| $R_{lshape}$ | Resistance of pulse shaping inductor             | 2.0 m $\Omega$  |
| $L_{shape}$  | Inductance of pulse shaping inductor             | 10 $\mu$ H      |
| $R_{cable}$  | Resistance of power cables                       | 5 m $\Omega$    |
| $L_{cable}$  | Inductance of power cable                        | 0.4 $\mu$ H     |

The circuit model for 200-kJ module is shown in Figure 3.17.

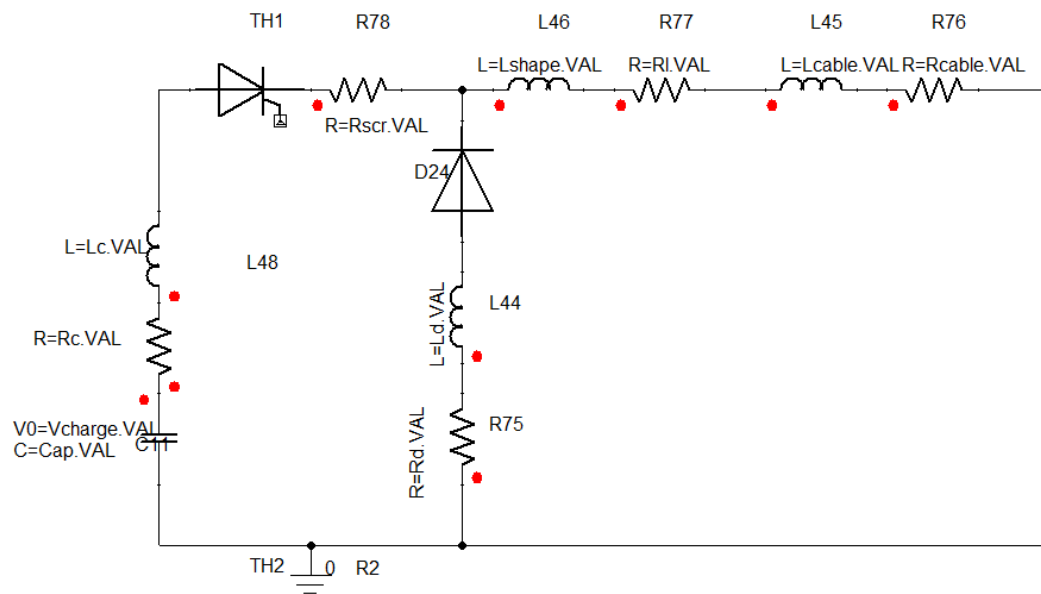


**Figure 3.17** Circuit model for 200-kJ unit module

Five 200-kJ unit modules are connected in parallel to form 1MJ PFU. The PFU is connected to a load that represents the rails and the armature. Load components are given in Figure 3.18.

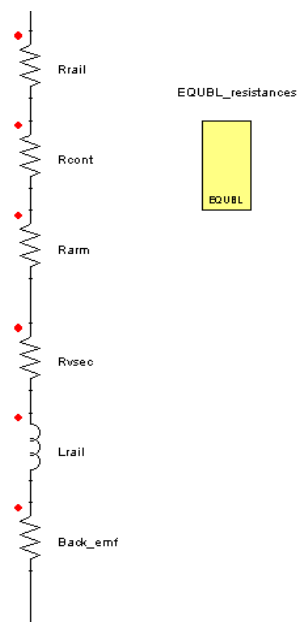


**Figure 3.18** Load components

The load includes rail resistance  $R_{\text{rail}}$ , contact resistance  $R_{\text{cont}}$ , armature resistance  $R_{\text{arm}}$ , velocity skin effect resistance  $R_{\text{vsec}}$ , rail inductance  $L_{\text{rail}}$  and a resistance that represents the back emf. The values for these components are found by implementing the equations given in section 3.1.1 and 3.1.2 in the equation block. Kinematic equations are also modeled in equation blocks. Velocity and position of the launch object are found using the blocks given in Figure 3.19.

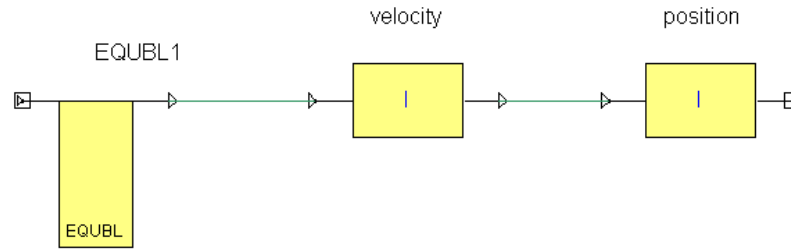


**Figure 3.19** Kinematic equation blocks

The current passing through the rail is used as the input for the equation block, as well as the mass and the inductance gradient defined by the user in the input section. As the acceleration of the launch object is found according to Equation 3.14, velocity and position are calculated by using integral blocks in the program.

The descriptions and the values of the parameters of PFU modules are given in Table 3.2. The remaining specifications of the simulated launcher are given in Table 3.3.

**Table 3.3** Specifications of the simulated EML

| Description                  | Value                |
|------------------------------|----------------------|
| Mass of the launch object    | 125 g                |
| Inductance gradient ( $L'$ ) | 0.45 $\mu\text{H/m}$ |
| Length of the rails          | 2 m                  |
| Width of the rails           | 25 mm                |
| Height of the rails          | 25 mm                |
| Distance between the rails   | 25 mm                |

Two different scenarios are simulated. Firstly, all 200 kJ unit-modules are triggered at the same time and the results are obtained and compared. Secondly, the modules

are triggered sequentially. Module trigger order for two scenarios is given in Table 3.4.

**Table 3.4** Module trigger order for two scenarios

| Scenario 1    |                   | Scenario 2    |                   |
|---------------|-------------------|---------------|-------------------|
| Module number | Trigger time (ms) | Module number | Trigger time (ms) |
| 1             | 0                 | 1             | 0                 |
| 2             | 0                 | 2             | 0                 |
| 3             | 0                 | 3             | 0.2               |
| 4             | 0                 | 4             | 0.6               |
| 5             | 0                 | 5             | 1                 |

Simulation results from two programs for scenario 1 are given in the Figs. 3.20-3.24 as below.

Figure 3.20 shows the current of module 1, which has a peak value of 149 kA with a rise time of  $t = 0.295$  ms. Total current passing through the rails, which corresponds to the sum of the current of five modules is given in Figure 3.21. The peak of the total current is approximately 746 kA, five times the peak of one module current as expected. The time when the launch object leaves the rails can be found from Figure 3.23. As the length of the rails is 2 meters, the moment the launch object position reaches 2 meters is the launch time. The launch time may also be decided from Figure 3.24. Total resistance of the rails and the launch object decays from a value. The time when this decaying path changes is the launch time because as in Equation 3.10 the rail resistance equation is defined as a piecewise function according to the rail length. In Figure 3.23 there is slight difference in launch time in two simulation results. In Simulink, the launch object leaves the rails at  $t = 5$  ms, whereas according to Simplorer the launch time is approximately 5.3ms. This difference arises from the difference in velocities obtained in two programs. As it may clearly be seen from Figure 3.22, the velocity of the launch object is higher in Simulink than the one in Simplorer solution. The velocity of the launch object is the integral of the acceleration and therefore, a closer look at the acceleration waveforms can explain the difference in the velocities found.

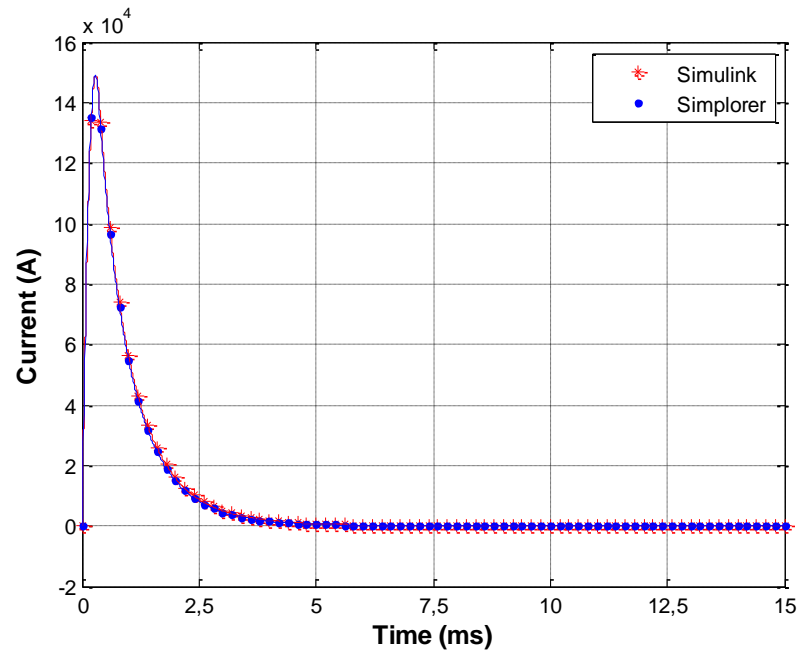


**Figure 3.20** Module 1 current

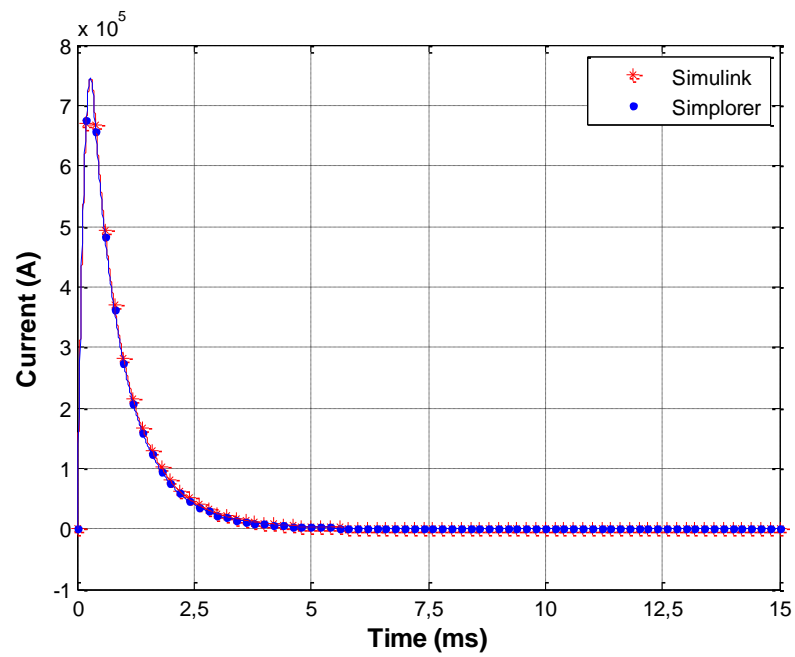


**Figure 3.21** Total current passing through the rails

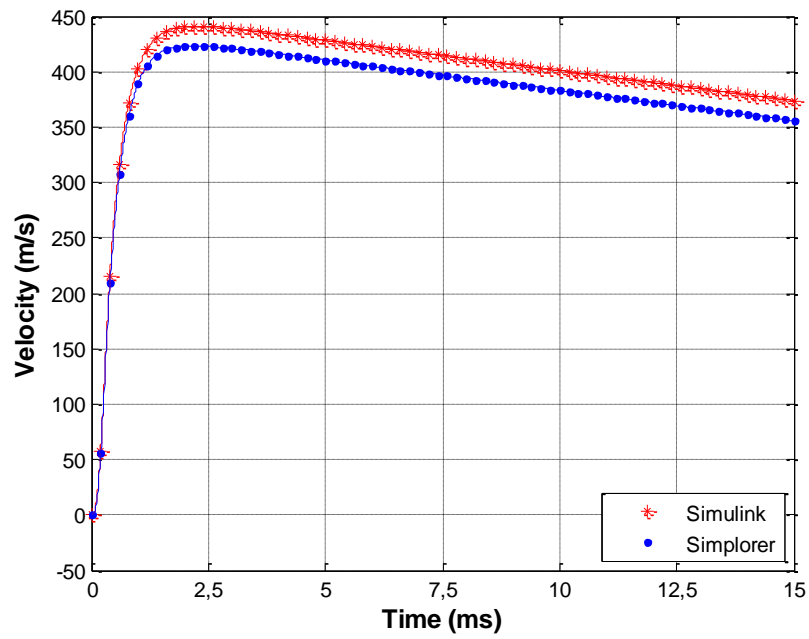


**Figure 3.22** Velocity of the launch object

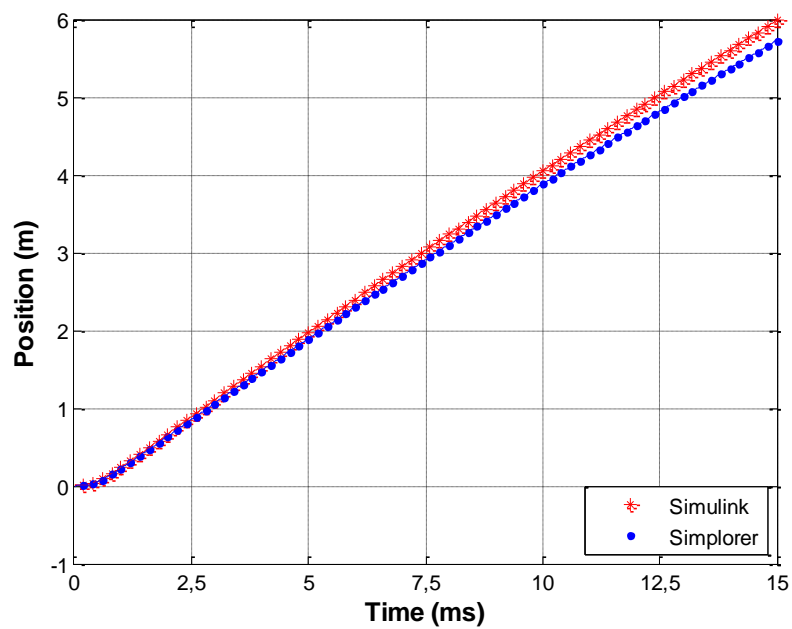


**Figure 3.23** Position of the launch object

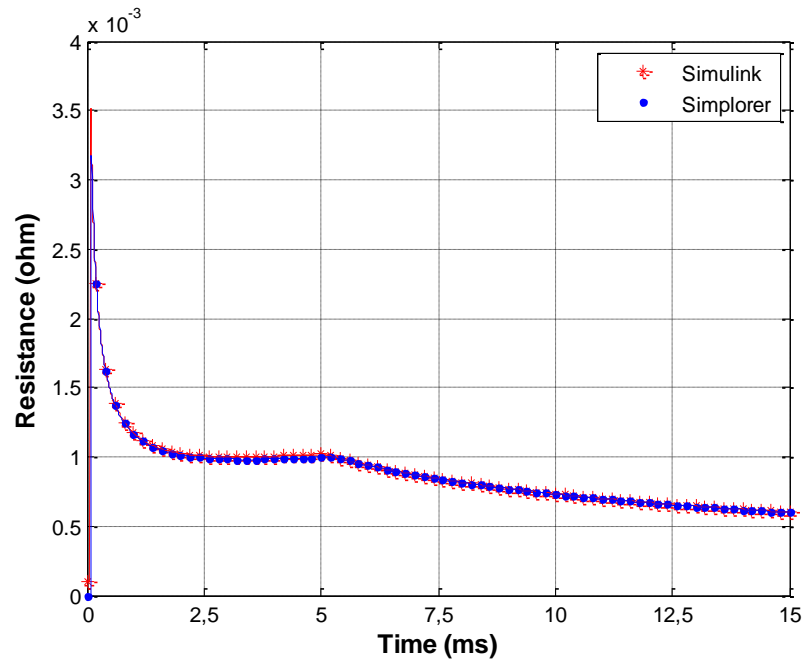


**Figure 3.24** Total resistance of the rails and the launch object

Figure 3.25 demonstrates the acceleration waveforms of the launch object. Although the difference between the peak values of the waveforms seems to be small, the figure scale is in the order of thousands and this results in 20-25 m/s difference in the maximum values of the velocity curves. However, according to Equation 3.14, Equation 3.16 and Equation 3.20, the main reason that lies behind these inequalities in acceleration, velocity and position waveforms in two programs is small differences between current waveforms given in Figure 3.21.

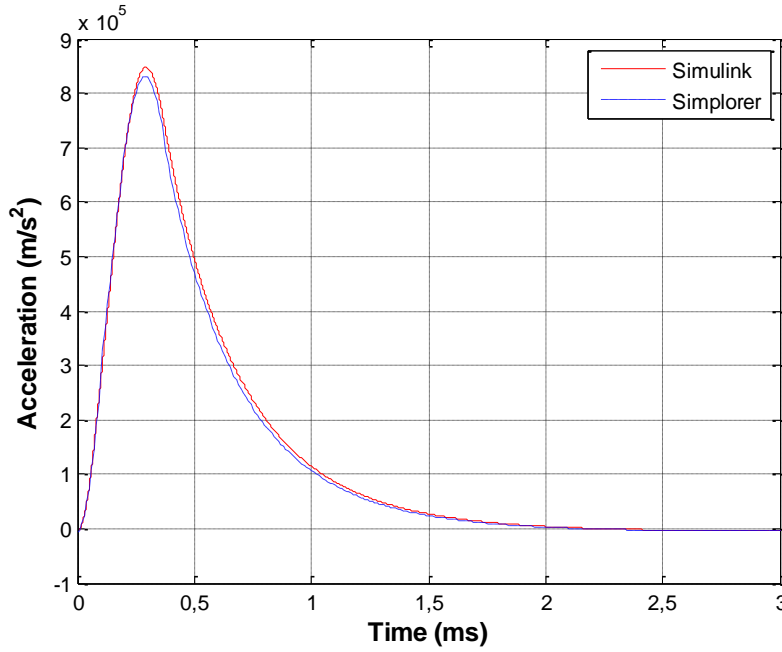


**Figure 3.25** Acceleration curves of the launch object

As stated before, a rectangular shape current pulse is preferred in EML applications. Therefore, instead of triggering all PFUs at once, a sequential triggering is applied. For this purpose, the same system is simulated again according to the timing sequence given in Table 3.4. Results are given in the Figs. 3.26-3.30 as below.

Figure 3.26 demonstrates the current of module-4. Module 4 is triggered at  $t = 0.6$  ms and has a peak value of 162 kA with a rise time of 0.3ms. Apart from trigger time, all the module currents have the same peak value and rise time. The total current passing through the rails is shown in Figure 3.27. It has a peak value of 430 kA and by sequential triggering, this value is kept almost constant for about 1 ms. The launch time may be found from Figure 3.30 as the instant when decaying path of the waveform changes and it is around 6.1 ms. The velocity and position waveforms found in two programs are noticeably different as shown in Figure 3.28 and Figure 3.29. The maximum values of the velocity and the position are higher in Simulink. The aforementioned reason for the differences in the same graphs in scenario 1 is still valid for the differences in scenario 2. However, the waveforms in Figure 3.28 are closer than waveforms in Figure 3.22 and the same is valid for the acceleration waveforms.



This means that inequalities in the total current waveforms shown in Figure 3.27 are less than the one in Figure 3.21.

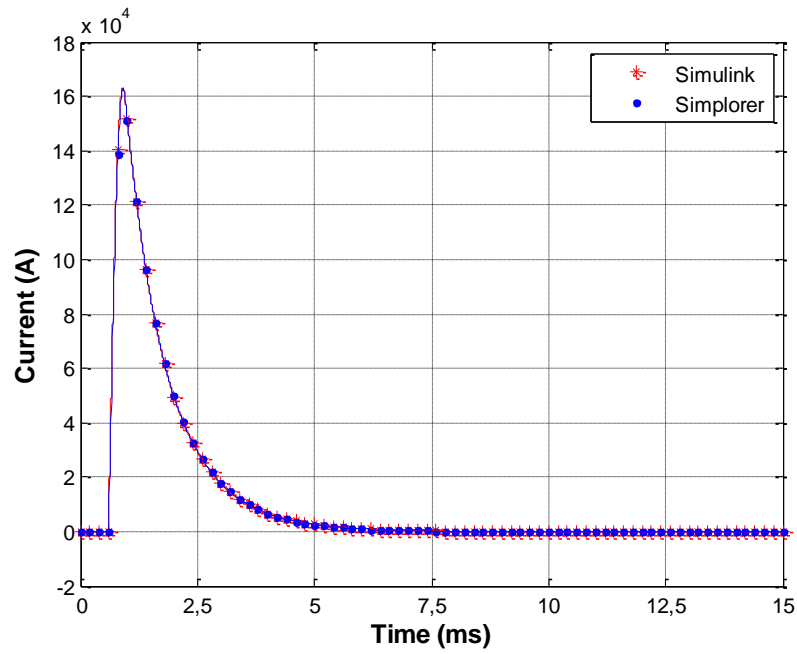


**Figure 3.26** Module 4 current

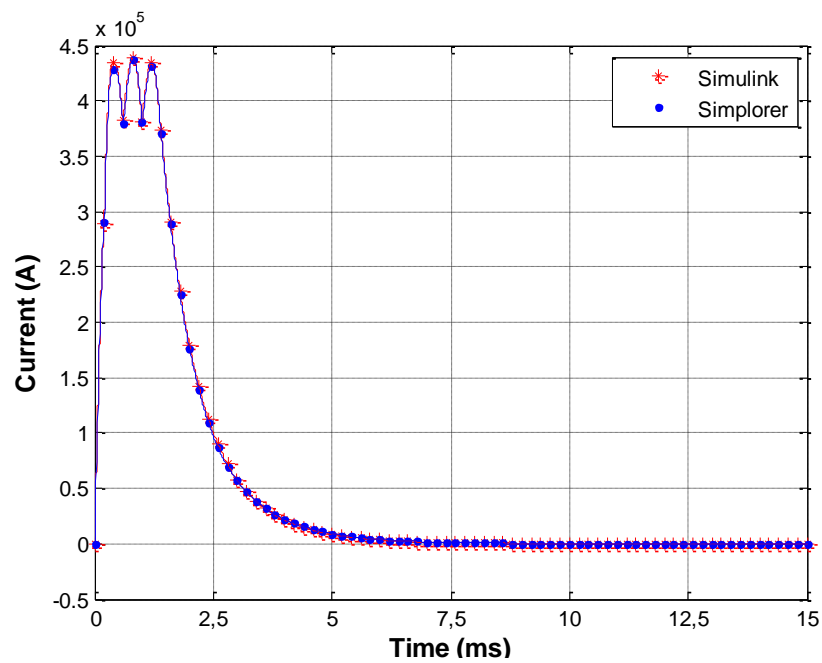


**Figure 3.27** Total current passing through the rails

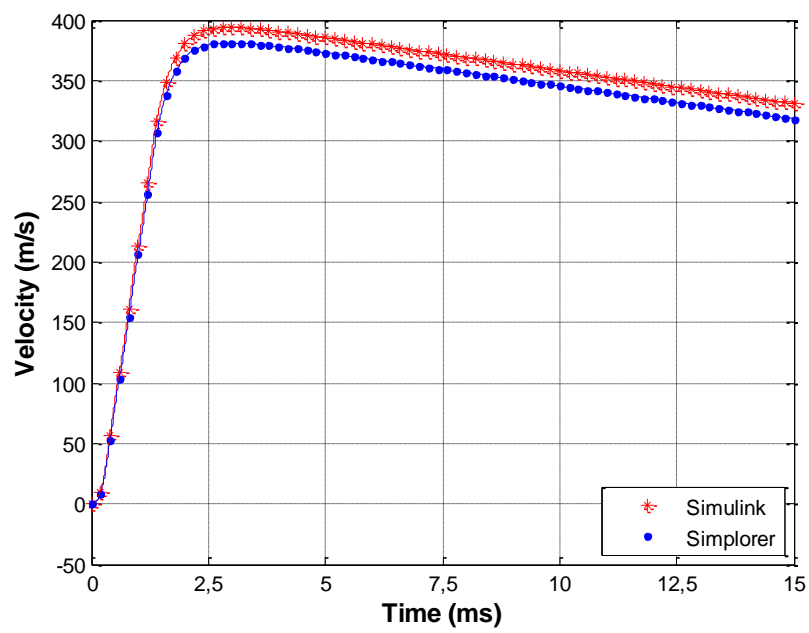


**Figure 3.28** Velocity of the launch object

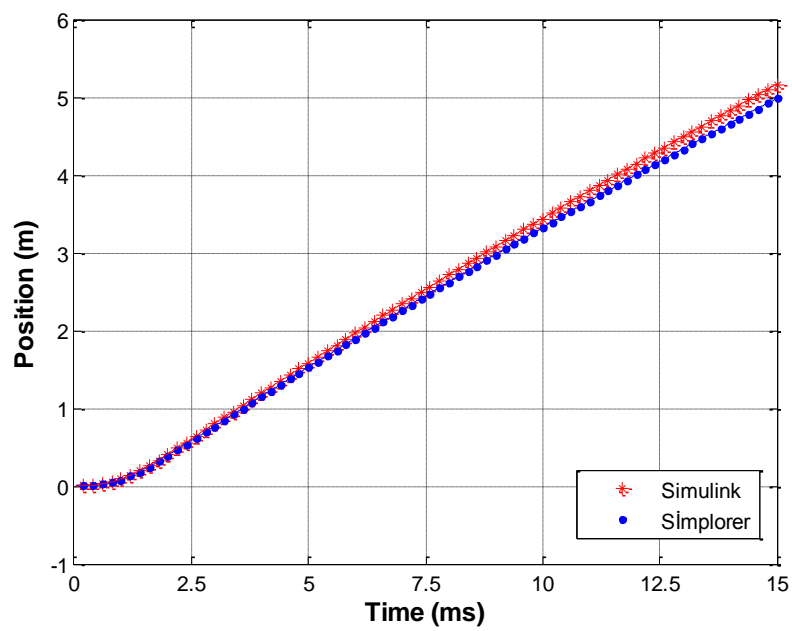


**Figure 3.29** Position of the launch object

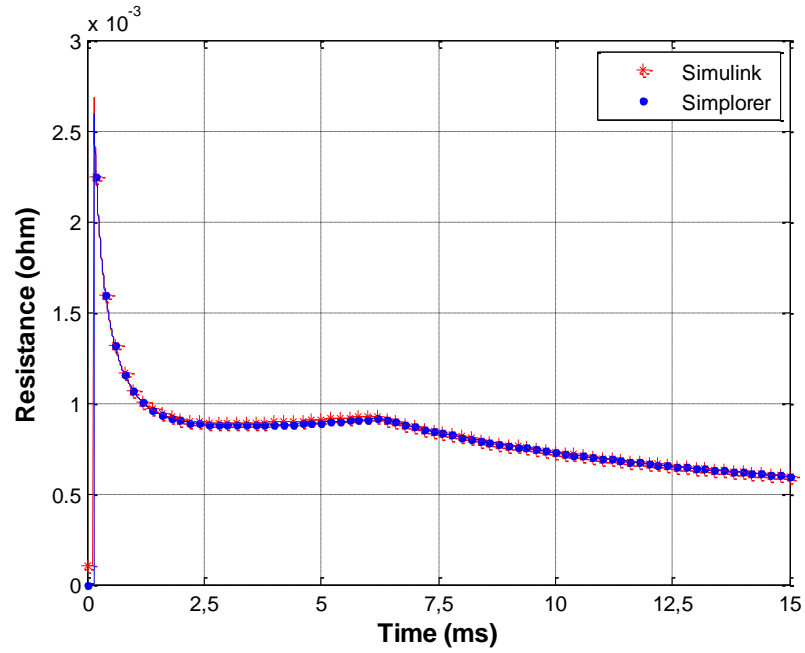


**Figure 3.30** Total resistance of the rails and the launch object

Some differences are noticed between the results for two scenarios. First of all, the peak value of the module current in scenario 2 is higher than the peak value of the module current in scenario 1. The reason may be explained through total resistance waveforms given in Figure 3.24 and Figure 3.30. Initial value of the resistance and the magnitude of the total current are higher in scenario 1. As a result, more energy is lost on resistance and total energy transferred to inductance is decreased. Consequently, peak value of the module current is less in scenario 1. Secondly, maximum values for the total current passing through the rails, the velocity and the position of the launch object are smaller in scenario 2 comparing to the values in scenario 1. Final and the most remarkable difference between the simulation results of two scenarios is seen in the waveforms of the total current passing through the rails. The current waveform in Figure 3.21 is a pulse current with a peak value of 746 kA while, in Figure 3.27, the current waveform consists of three pulse currents with the same peak value around 430 kA. A flat current waveform is observed in scenario 2 because of sequential triggering. Since the Lorentz force is directly proportional to the square of the current passing through the rails, the maximum value for the velocity of the launch object is higher in scenario 1, but this difference is about 30 m/s. On the other hand, the difference in the peak values of the total current between two scenarios is nearly 320

kA, which causes higher deformation of the material of the rails and the launch object for the scenario 1 as compared to scenario 2. Furthermore, rail dimensions have to be expanded as the amount of current passing through the rails increases and this results in higher costs. Therefore, sequential triggering is preferred generally in EML applications.

## CHAPTER 4

### EXPERIMENTAL PROCEDURE

#### 4.1. Experimental Goals

In the previous chapter, EML is modeled in two different simulation environments. In order to continue with further studies using simulations, the models have to be verified by experimental results. For this purpose, a system similar to an EML is prepared. Instead of rails and launch object, a sliding contact mechanism is connected to PFU as a load. Several tests are performed and data is recorded. The models mentioned in previous chapter are modified to simulate the system used in the experiment. Finally, simulation and experimental results are compared.

#### 4.2. Experimental Components

The system used in the experiment is composed of two parts: a PFU and a load. PFU includes a capacitor bank, a pulse shaping inductor and a crowbar diode bank. Capacitors are charged to desired voltage level through a DC voltage source. Circuit schematic of the PFU and the voltage source is given in Figure 4.1.

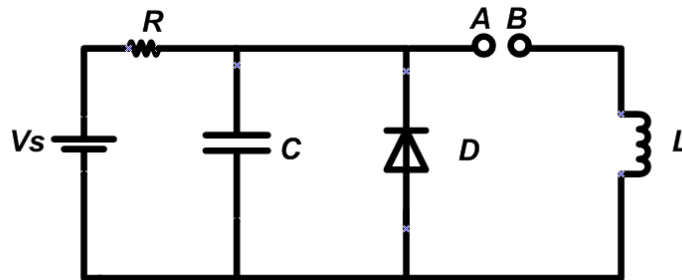


**Figure 4.1** Circuit schematic of the PFU and DC voltage source

Unlike PFUs generally used in EML application, there is not an external switching unit in this PFU. Circuit is closed by the sliding mechanism in the load. Load is

connected to the PFU from A and B terminals shown in Figure 4.1. A special load is designed to represent rails and launch object in an EML. In EML, launch object slides between the rails with electromagnetic force acting on it. During the motion, due to very high currents passing through the rails and the launch object, erosion and degradation occur in conductors. Moreover, contact between these two weakens. If the contact between the rails and the launch object is set to be poor initially, as the launch object moves along the rails contact is lost and arcing occurs, resulting in high resistances. By taking these issues into consideration, the mechanism given in Figure 4.2 is developed.

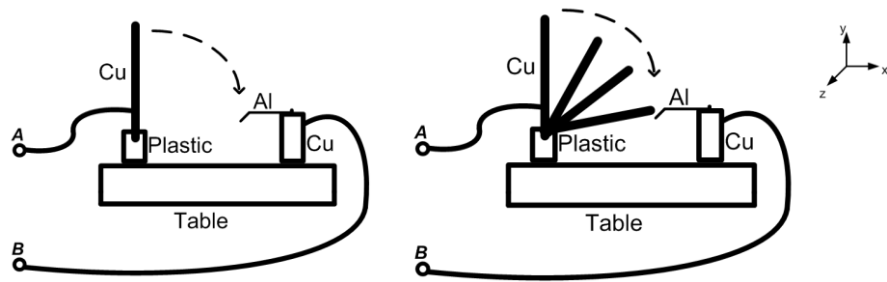


**Figure 4.2** Schematic (left ) and rotation axis (right) of the mechanism designed to represent the rails and the launch object

This mechanism includes a copper rod screwed between two non-conducting L shape plastic materials. It can rotate around z axis. Copper rod is wired to the PFU from terminal A shown in Figure 4.1. On the other end of the table, aluminum is screwed to copper and placed on the route of the copper rod such that it hits the edge of the aluminum and a copper-aluminum contact is formed. Terminal B, which is shown in Figure 4.1, is wired to copper. It is expected that as the copper rod gets close enough to the aluminum, arcing occurs and PFU circuit is closed. After a short time, the rod hits the aluminum and contact is formed. Then due to high current, aluminum melts from the edge and contact is lost. After contact loss, a short arcing occurs again and finally conduction stops. Therefore, a time varying resistance is expected to be observed in the load. Circuit schematic of the overall system is presented in Figure 4.3.

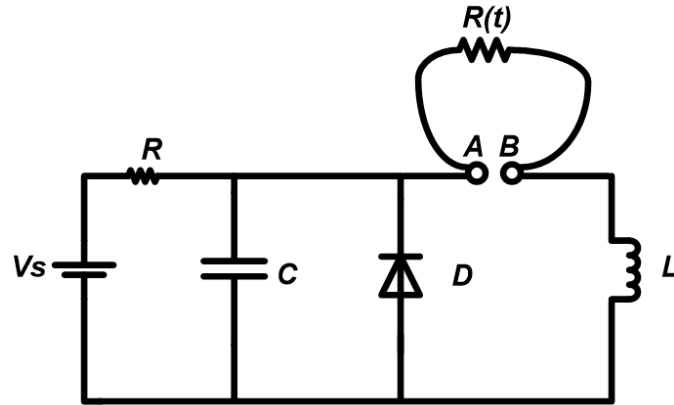


**Figure 4.3** Circuit schematic of the system

Aluminum samples are 10 cm long and width of the samples are changed during the experiment. Samples having a width of 0.6 cm and 1 cm are used in experiments in order to see the effect of the aluminum width on the load resistance. One edge of the aluminum is curved to increase contact area between aluminum and copper. The load and aluminum samples used in the experiment are shown in the figures below.

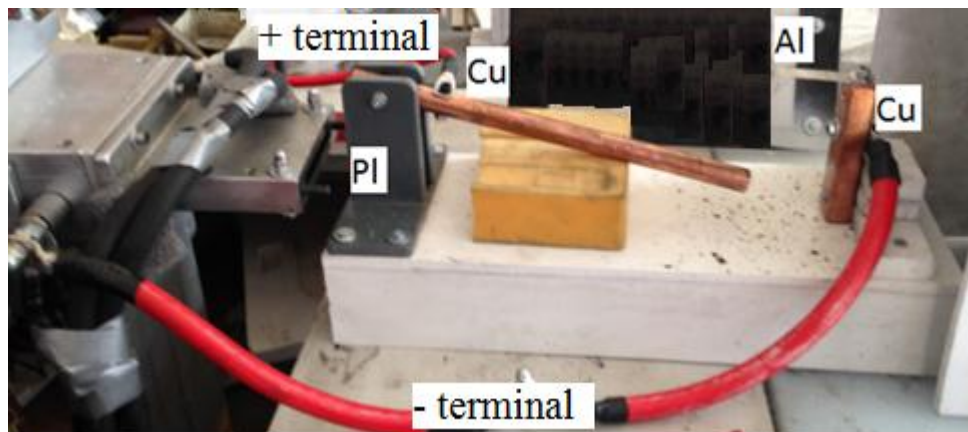


**Figure 4.4** Load used in the experiment



**Figure 4.5** Aluminum samples used in the experiment

### 4.3. Data Acquisition

The main aim in the experiment is to obtain required data to model the electrical resistance of the load and use it in the simulation. Measurements are performed accordingly. Electrical resistance between two nodes can be explained as the ratio of voltage between the nodes to current passing through the nodes. Therefore, measuring the voltage between A and B nodes given in Figure 4.3 and the current passing through the load would be adequate to find the resistance. Schematic of measurements is given in Figure 4.6.

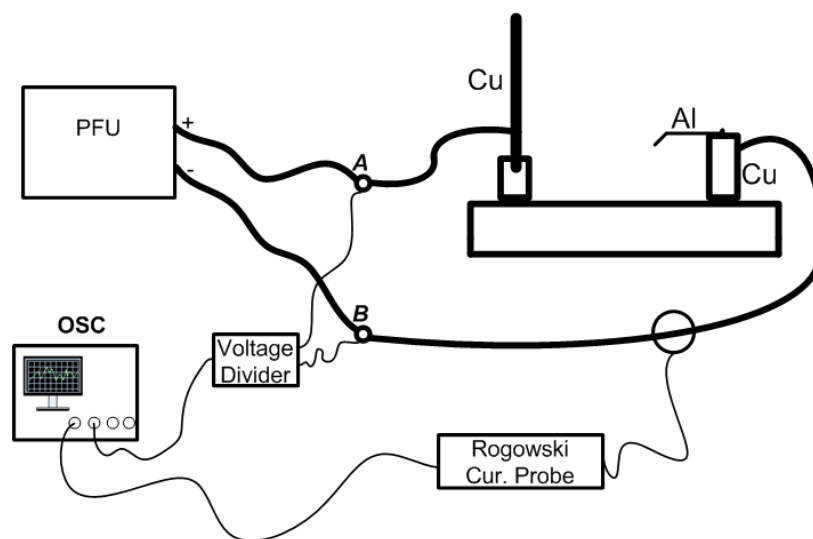


**Figure 4.6** Schematic of measurements



Voltage divider used in the experiment is a capacitive voltage divider and has a ratio of 1:20. Current is measured by Rogowski current probe. Rogowski current probe is generally used for transient current measurements. It consists of an air-cored coil which is named as Rogowski coil and an integrator. It is placed around a current-carrying conductor. As the current passing through the conductor changes, a voltage is generated on the coil. This voltage is proportional to the rate of change of current. The voltage is then integrated to find the flux linkage which is proportional to the current. Basic form of a Rogowski current probe is shown in Figure 4.7.

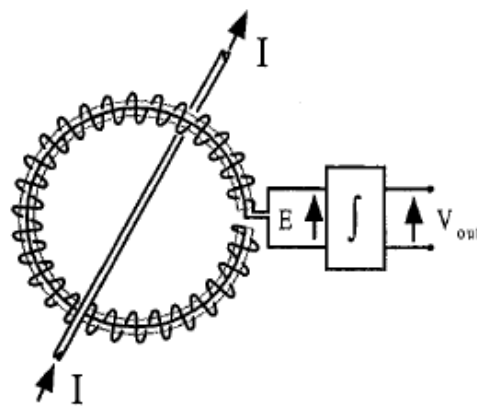


**Figure 4.7** Basic form of Rogowski current probe [35]

During the experiments, a commercially available Rogowski Current Probe (PEM CWT 300LFB) is used. The probe has 0,1mV/A ratio. More information about Rogowski probe is provided in APPENDIX A. Voltage and current signals are monitored and saved by Tektronix DPO3034 oscilloscope. Measurement equipments are shown in Figure 4.8.

#### 4.4. Test Procedure and Results

Components of the experimental setup are shown in Figure 4.8 and Figure 4.9.

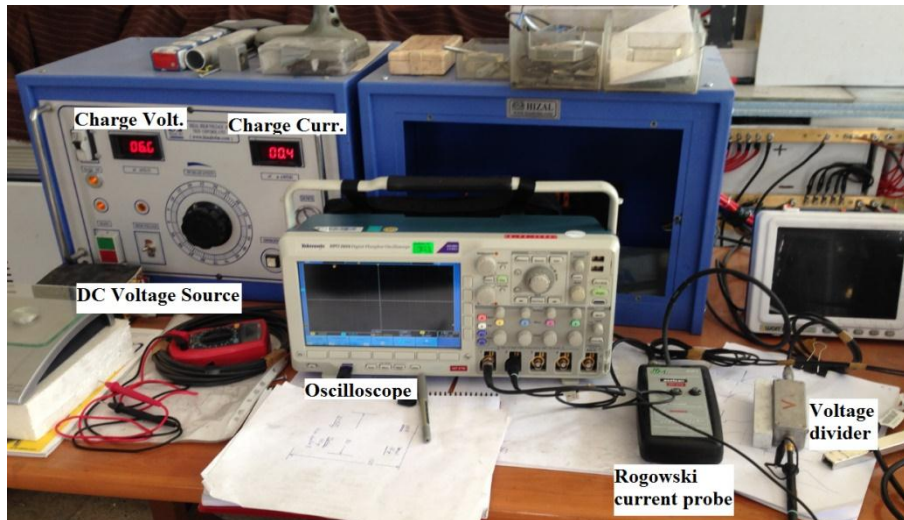


**Figure 4.8** DC Voltage source, oscilloscope and probes

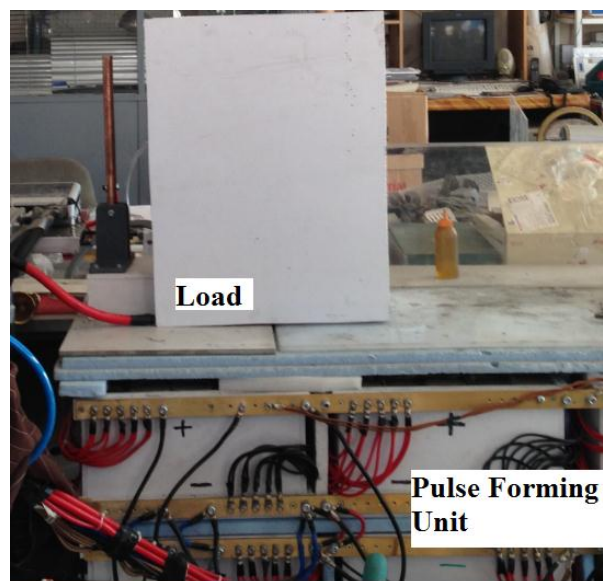


**Figure 4.9** Pulse Forming Unit and load

The capacitor bank in the PFU shown in Figure 4.9 is produced by connecting several 100  $\mu\text{F}$ , 650 V capacitors in parallel so that total capacitance of the PFU is 200 mF. The energy of the PFU is 42.25 kJ, if capacitors are charged to 650 VDC. However, capacitors are charged to 100 VDC in the experiment since that amount of charge voltage is enough to create current pulse to melt aluminum. The crowbar diode pack

is also produced by connecting 70A, 1200 V diodes both in parallel and series so that the resulting diode pack withstands 35000 A, 20 ms pulse currents according to their ratings. Inductance of the pulse shaping inductor is 663  $\mu$ H.

Test procedure simply includes charging of the capacitors and closing the circuit by pushing the copper rod manually. As the circuit is closed by copper-aluminum interaction, both voltage and current of the load is monitored and data is recorded. The load is enclosed by a box to prevent scattering of aluminum particles over test area as shown in Figure 4.9. Several aluminum plates are used in the experiments. However, due to poor arrangement of the aluminum plates' position, some unexpected waveforms are observed as shown in Figure 4.10. Ripples in the voltage waveform prevent to make reliable analyses about what is really happening between the aluminum plate and the copper rod.

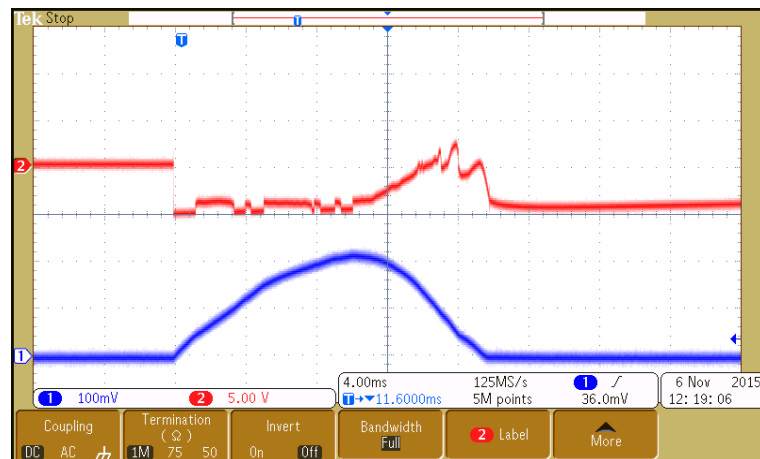


**Figure 4.10** Waveforms for poorly adjusted aluminum-copper contact (CH1: Blue, Current, 1kA/div, CH2: Red, Voltage 100V/div)

After some trials, the most appropriate aluminum plate position is found and following waveforms are observed.

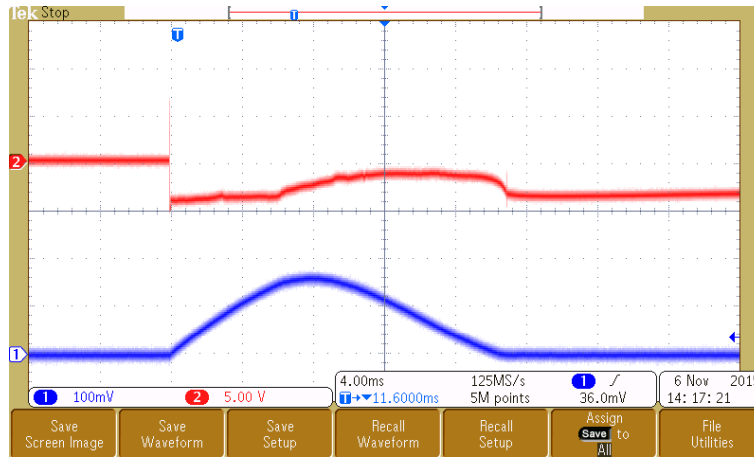


**Figure 4.11** Waveforms for well-adjusted aluminum-copper contact  
(CH1: Blue, Current, 1kA/div, CH2: Red, Voltage 100V/div)

Experiments are also repeated for 0.6 cm wide aluminum plates and same waveforms are observed as shown in Figure 4.12. This means that change in the resistance of the aluminum plate doesn't significantly affect the load resistance. There are other dominant resistances that build up the load resistance.

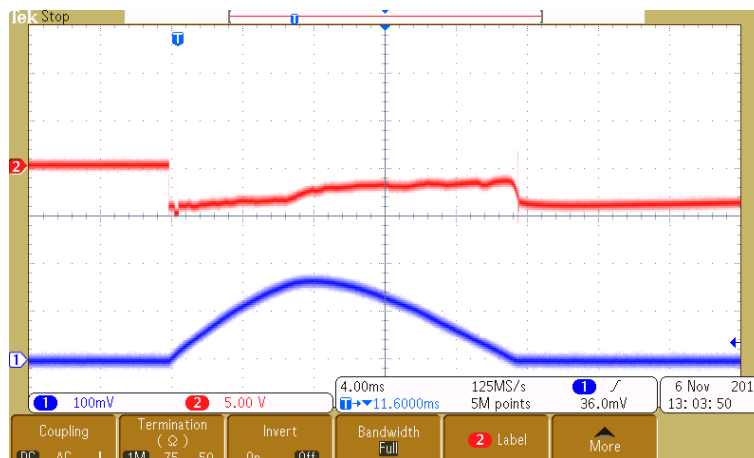


**Figure 4.12** Waveforms for well-adjusted aluminum-copper contact for 0.6 cm wide aluminum plate  
(CH1: Blue, Current, 1kA/div, CH2: Red, Voltage 100V/div)

The copper rod and aluminum plates are deformed through the experiments as shown in Figure 4.13. Peak values of the currents passing through the load are observed to be between 1.5-2 kA. This gives the idea of how could rail and armature material be affected by peak currents of hundred thousand kA in an actual EML application.



**Figure 4.13** Deformation in the copper rod and aluminum plates

#### 4.5. Data Analysis

Results of successful trials are analyzed to find the load resistance. Current pulse is observed between 8 ms and 26 ms time interval in oscilloscope recordings as shown in Figure 4.11 and Figure 4.12. A resistance waveform for this time interval is found by dividing voltage to current as demonstrated in Figure 4.14.

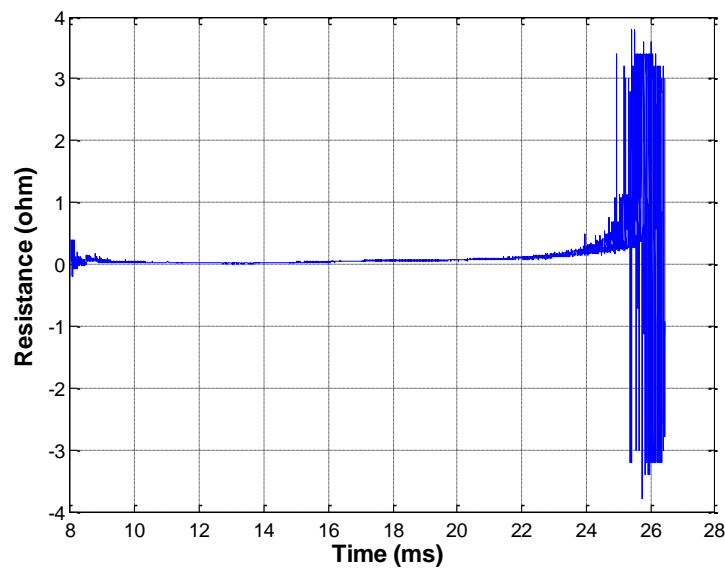


**Figure 4.14** Resistance waveform for the time interval between 8ms and 26 ms

The waveform in Figure 4.14 doesn't give enough information about the load resistance. However, it may be said that resistance is high at the beginning and at the

end of the time interval. A closer look at the waveform is needed to see the exact characteristic of the load resistance. Therefore, the time interval is narrowed between 10 ms and 24 ms and the waveform in Figure 4.15 is obtained.

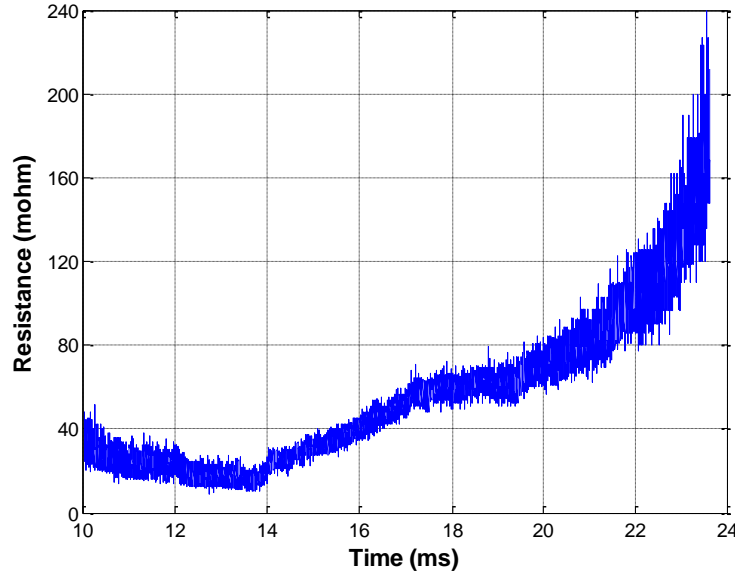


**Figure 4.15** Resistance waveform for the time interval between 10 ms and 24 ms

As there is contact between two different materials and the peak value of current passing through these materials is very high, we can not say that the load resistance is simply composed of copper and aluminum resistances. It includes different components between different time intervals. At  $t = 10ms$  a contact is formed between aluminum plate and copper rod, in other words, copper rod touches aluminum plate. Initial resistance is  $40m\Omega$ . Between  $t = 10ms$  and  $t = 14ms$  contact area increases and therefore resistance decreases. At the same time, aluminum temperature increases. At  $t = 14ms$ , aluminum melts and plasma occurs. Resistance between  $t = 14ms$  and  $t = 24ms$  is the sum of calescent aluminum resistance and plasma resistance. The value of the current decreases as time passes and plasma length and plasma resistance increases. At  $t = 26ms$ , conduction stops and plasma vanishes.

The next step is to validate the simulation with the experimental data. Waveform in Figure 4.15 is used to model the load resistance. To do this, curve fitting function of MATLAB is applied to the waveform and an equation for the resistance is derived.

Curve fitting waveform together with actual resistance waveform are given in Figure 4.16.

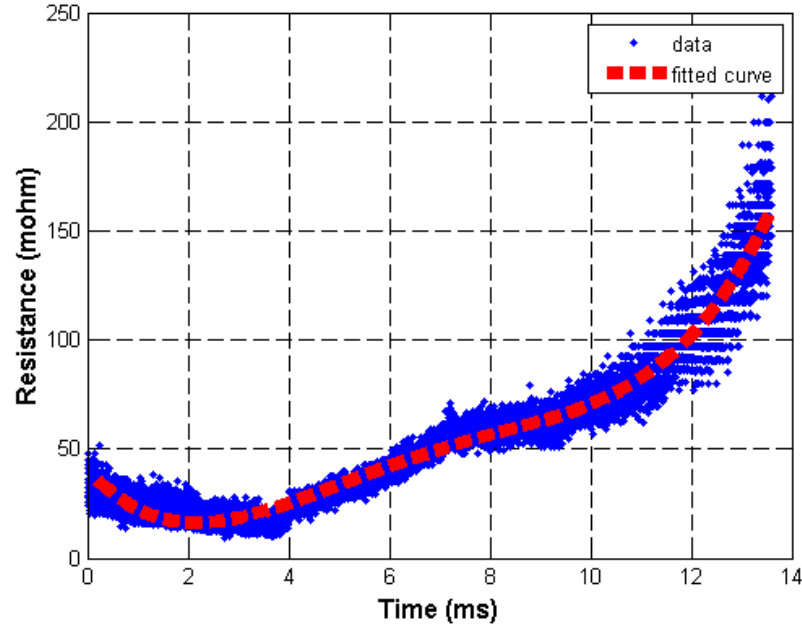


**Figure 4.16** Curve fitting waveform and actual waveform

Equation for the load resistance as a result of curve fitting is

$$R(t) = 3.863 \times 10^8 t^4 - 9.674 \times 10^6 t^3 + 8.945 \times 10^4 t^2 - 265.6t + 0.4075 \quad (4.1)$$

Simulation models of the system is prepared in two simulation environments by modifying the models given in 3.3 and 3.4. The system in the experiment includes one PFU and a resistive load. Therefore, input blocks are reduced to include parameters shown in Figure 4.17 and Figure 4.18.

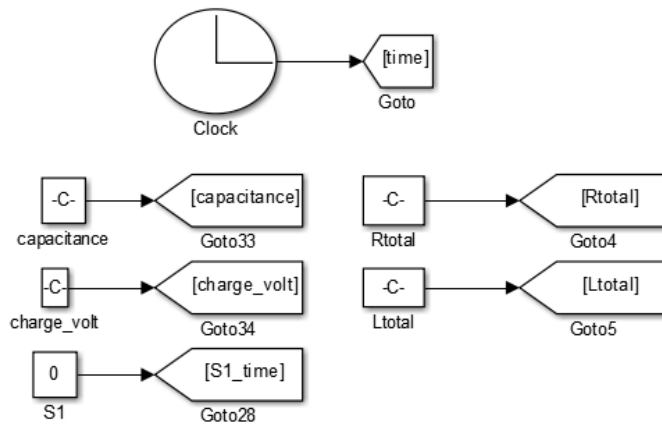


**Figure 4.17** Input parameters for the system in Simulink

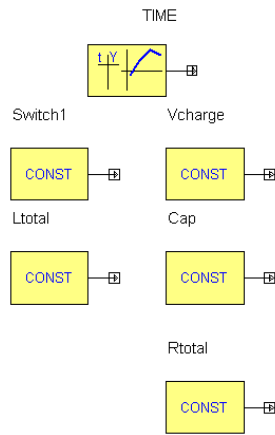


**Figure 4.18** Input parameters for the system in Simplorer

Module voltage and current are calculated by the blocks demonstrated in Figure 4.19 in Simulink. On the other hand, circuit schematic shown in Figure 4.20 is used to find module voltage and current in Simplorer.



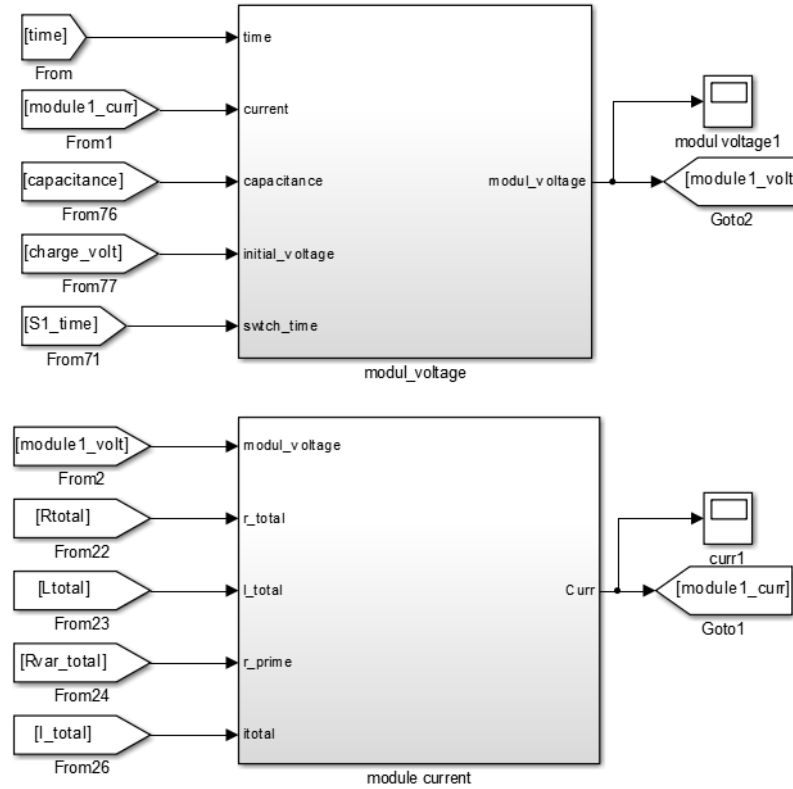


**Figure 4.19** Module voltage and module current block in Simulink

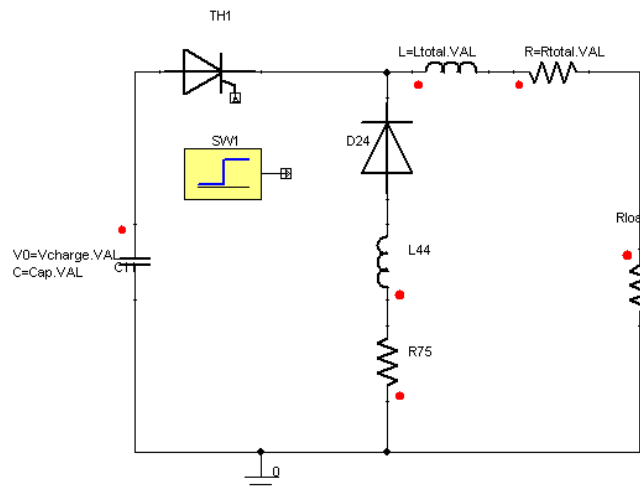


**Figure 4.20** Circuit schematic in Simplorer

Finally, load resistance is modeled by implementing Equation 4.1 in the model as shown in Figure 4.21 and Figure 4.22.

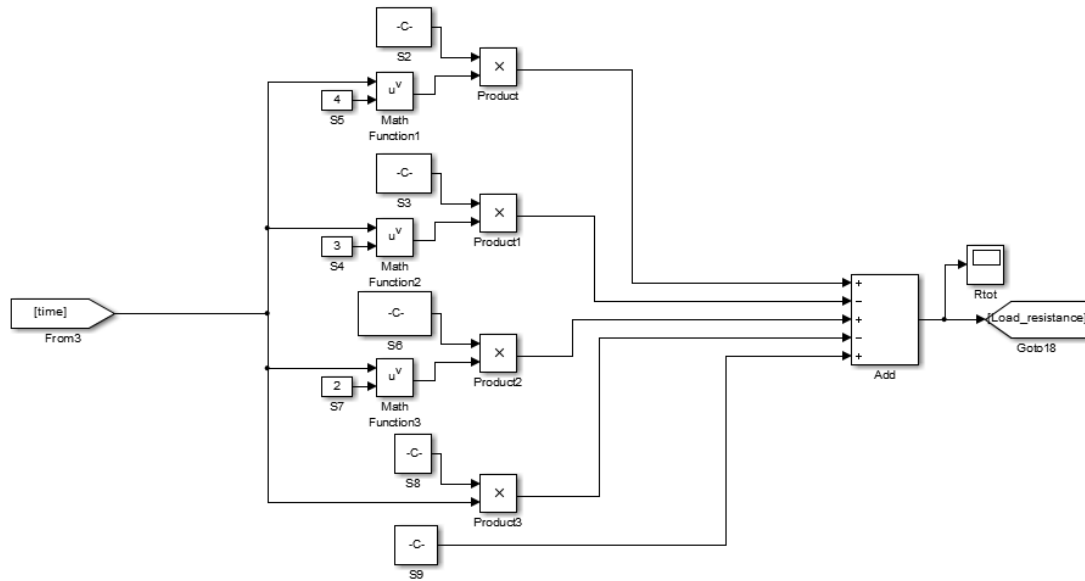


**Figure 4.21** Implementation of load resistance model in Simulink

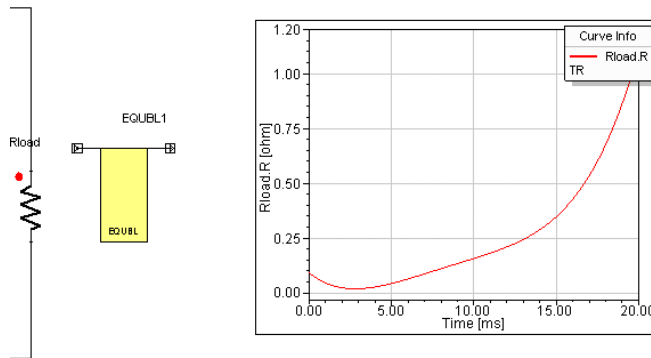


**Figure 4.22** Implementation of load resistance model in Simplorer

Simulations are run according to input parameter values given in Table 4.1. The current waveforms are compared with the experimental result. The experimental and simulated current waveforms are shown in Figure 4.23.

**Table 4.1** Input parameter values used in the simulation

| Input Parameter    | Value           |
|--------------------|-----------------|
| Capacitance        | 200 mF          |
| Charge voltage     | 100 V           |
| $R_{\text{total}}$ | 5.25 m $\Omega$ |
| $L_{\text{total}}$ | 663 $\mu$ F     |

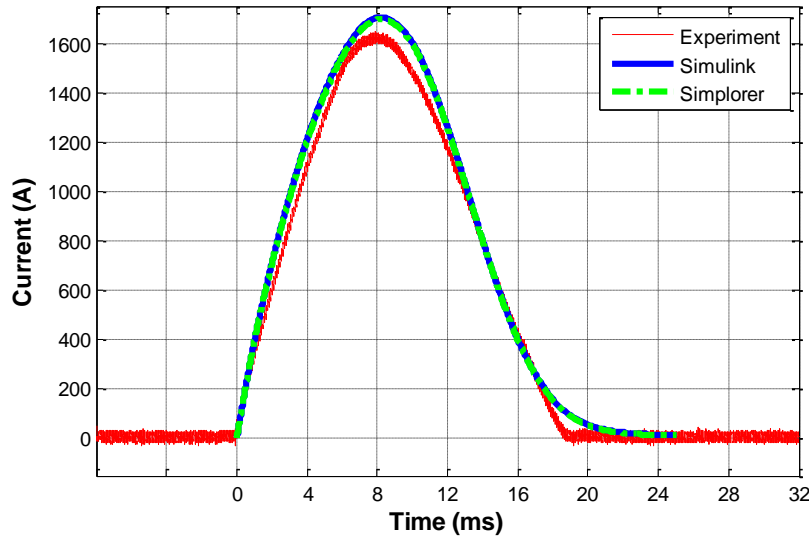


**Figure 4.23** Comparison of the current curves

Simulink and Simplorer simulation results agree with each other. However, simulation results have little error compared with the measured value. The rise time is shorter and the peak value of the pulse current is less for the experimental curve as compared to simulation curves. The difference may be explained by comparing resistance waveforms in Figure 4.14 and Figure 4.16. High resistance observed around 8 ms in Figure 4.14 is not included in deriving model for the load resistance. This high resistance at the beginning results in higher heat loss. In addition, the amount of energy that is transferred to inductance decreases. As a result, peak value of the current and rise time decreases. Another difference is observed at the tails of the pulses. Fall time for the experimental curve is lower than fall time for the simulation curves. The reason again lies in the difference between resistance curves given in Figure 4.14 and Figure 4.16. Very high resistances that occur around  $t = 25\text{ms}$  causes a faster discharge in the experiment. These high resistances again are not included in the resistance model of the load. However, errors of simulations are within an acceptable scale of 5%.



## CHAPTER 5

### CONCLUSION

There is a growing interest in electromagnetic launch applications worldwide. Several institutions and companies are producing prototypes and doing research on developing electromagnetic launch technology. Research efforts spread over a wide range of areas. Material technology, energy storage, power conditioning, modeling are areas where electromagnetic launch studies mainly focus on. A collaborative study is needed to conduct development studies because there are a lot of different mechanisms that effect the overall performance of the system. Moreover, these studies should be supported by simulation and modeling efforts. An experimentally validated simulation may be used to predict the result of change in each parameter on the overall performance of the system instead of conducting an experiment.

The framework of this thesis is to develop an electromagnetic launcher model. Two different models are prepared to be able to analyze system from different aspects. These models take all of the variables affecting the performance of the system into account. Each variable can be controlled and result of the change in each variable can be observed through simulations. Simulation studies are also supported by experimental results.

In the first chapter, an overview of EML and EML applications has been provided. Information about EML research studies worldwide is presented.

In the second chapter, electromagnetic launcher components have been elaborated. Additionally, Lorentz force, where electromagnetic launch technology is founded on, is simplified to the well-known equation  $F = \frac{1}{2} L' I^2$  using electromagnetic launch theory and Biot-Savart law. Finally, brief information on modeling of electromagnetic launcher is given. Different methods and simulation approaches applied in the literature are stated.

Third chapter has started with deriving all the equations governing both electrical and kinematic models of the electromagnetic launcher. Two simulation models are developed in MATLAB/Simulink and Simplorer simulation programs. A new approach used in Simulink model. Two different current paths are defined while deriving current equation instead of using only one path that is applied in both [20], [22]. By this way, freewheeling diode impedance is taken into account. Additionally, change in the impedances of capacitor and high voltage switch would only effect the rise time of the current. In the next step, simulation results for the same system is obtained and compared. The results have seemed to be quite similar except small differences in velocity and position curves. Next, the reason of the difference is discussed in detail.

Finally, in the fourth chapter, an experimental test set up has been presented. Test set up does not fully represent an electromagnetic launcher; however, models are modified to simulate the system used in the experiment. Firstly, experiments are conducted and results are monitored and recorded. After that, resistance model of the load is found through some analysis in Simulink. Finally, resistance model is implemented in two simulation programs and current waveforms of both simulations and experiment are compared. Since the resistance model does not include high resistances observed at the beginning and at the end of the conduction in the experiment, rise time and peak value of the current waveform are smaller in the experimental curve.

This work is open to different perspectives, since the models used in this work is designed for general purpose pulse power applications. The approach used to find the load resistance model will be applied to obtain the rail and launch object resistance models in a real electromagnetic launch application. EML models built in two simulation programs need to be fully validated with experiments conducted with a real electromagnetic launcher.

Another step would be building of a GUI for electromagnetic launcher simulations. User provides all inputs defined for the system and GUI shows all resultant waveforms of the simulation. Owing to this, all of the efforts will gain a professional look.

## REFERENCES

- [1] Kory A. Swope, "Prediction of Electromagnetic Launcher Behavior with Lubricant Injection Through Armature-Rail Interface Modeling," Master's thesis, Georgia Institute of Technology, Atlanta, Georgia, May 2010.
- [2] A.Pullen, L. Qiao and S. Sawyer, "Global Wind Report 2013– Market Forecast 2014-2018", Global Wind Energy Council GWEC, Brussels, Belgium, March 2013.
- [3] Hundertmark, S., "Applying railgun technology to small satellite launch," in Recent Advances in Space Technologies (RAST), 2011 5th International Conference on , vol., no., pp.747-751, 9-11 June 2011
- [4] "Atlas V Launch Services User's Guide March 2010," United Launch Alliance, March 2010, pp. 1-5
- [5] Schneider, M.; Božić, O.; Eggers, T., "Some Aspects Concerning the Design of Multistage Earth Orbit Launchers Using Electromagnetic Acceleration," in Plasma Science, IEEE Transactions on , vol.39, no.2, pp.794-801, Feb. 2011
- [6] McNab, I.R.; LeVine, F.; Aponte, M., "Experiments with the Green Farm electric gun facility," in Magnetism, IEEE Transactions on , vol.31, no.1, pp.338-343, Jan. 1995
- [7] Hammon, H.G.; Dempsey, J.; Strachan, D.; Raos, R.; Haugh, D.; Whitby, F.P.; Holland, M.M.; Eggers, P., "The Kirkcudbright Electromagnetic Launch Facility," in Magnetism, IEEE Transactions on , vol.29, no.1, pp.975-979, Jan 1993

- [8] Satapathy, S.; McNab, I.R.; Erengil, M.; Lawhorn, W.S., "Design of an 8-MJ integrated launch package," in *Magnetics, IEEE Transactions on* , vol.41, no.1, pp.426-431, Jan. 2005
- [9] Wegner, V.; Jamet, F., "Electromagnetic acceleration activities at the French-German Research Institute Saint-Louis (ISL)," in *Magnetics, IEEE Transactions on* , vol.25, no.1, pp.587-590, Jan 1989
- [10] Wey, J.; Lehmann, P.; Peter, H., "DES 3 MJ-railgun experimental results at ISL," in *Magnetics, IEEE Transactions on* , vol.31, no.1, pp.371-376, Jan. 1995
- [11] Lehmann, P.; Peter, H.; Wey, J., "First experimental results with the ISL 10 MJ DES railgun PEGASUS," in *Magnetics, IEEE Transactions on* , vol.37, no.1, pp.435-439, Jan 2001
- [12] Schneider, M.; Woetzel, M.; Wenning, W.; Walch, D., "The ISL Rapid Fire Railgun Project RAFIRA Part I: Technical Aspects and Design Considerations," in *Electromagnetic Launch Technology, 2008 14th Symposium on* , vol., no., pp.1-6, 10-13 June 2008
- [13] Hundertmark, S.; Schneider, M.; Vincent, G., "Payload Acceleration Using a 10-MJ DES Railgun," in *Plasma Science, IEEE Transactions on* , vol.41, no.5, pp.1455-1459, May 2013
- [14] Jun Li; Shizhong Li; Peizhu Liu; Yingchun Gui; Ning Su; Jiannian Dong; Jun Zhang; Yinghui Gao; Weiqun Yuan; Ping Yan, "Design and Testing of a 10-MJ Electromagnetic Launch Facility," in *Plasma Science, IEEE Transactions on* , vol.39, no.4, pp.1187-1191, April 2011
- [15] Ling Dai; Yanzhao Wang; Qin Zhang; Wenting Li; Wanxin Lu; Hanbin Dong; Fuchang Lin, "Effect of sequence discharge on components in a 600kJ PPS



used for electromagnetic launch system," in Electromagnetic Launch Technology (EML), 2012 16th International Symposium on , vol., no., pp.1-6, 15-19 May 2012

- [16] Zizhou Su; Wei Guo; Tao Zhang; Honghai Zhang; Zhiqiang Dong; Junyi Yang; Bin Cao, "Design and Simulation of a Large Muzzle Kinetic Energy Railgun," in Plasma Science, IEEE Transactions on , vol.41, no.5, pp.1416-1420, May 2013
- [17] Young-Hyun Lee; Seong-Ho Kim; Byung-Ha Lee; Sanghyuk An; Kyung-Seung Yang, "Experimental tests of a 25mm square-bore railgun," in Electromagnetic Launch Technology (EML), 2012 16th International Symposium on , vol., no., pp.1-6, 15-19 May 2012
- [18] Yun Sik Jin; Young Bae Kim; Jong Soo Kim; Chuhyun Cho; Soo Won Lim; Byungha Lee; Sung Ho Kim; Sanghyuk An; Seok Han Yoon; In Su Koo, "Fabrication and Testing of a 600-kJ Pulsed Power System," in Plasma Science, IEEE Transactions on , vol.41, no.10, pp.2671-2674, Oct. 2013
- [19] Kyung-Seung Yang; Seong-Ho Kim; Byungha Lee; Sanghyuk An; Young-Hyun Lee; Seok Han Yoon; In Su Koo; Yun Sik Jin; Young Bae Kim; Jong Soo Kim; Chuhyun Cho, "Electromagnetic Launch Experiments Using a 4.8-MJ Pulsed Power Supply," in Plasma Science, IEEE Transactions on , vol.43, no.5, pp.1358-1361, May 2015
- [20] Taher, S.A.; Jafari, M.; Pakdel, M., "A New Approach for Modeling Electromagnetic Railguns," in Plasma Science, IEEE Transactions on , vol.43, no.5, pp.1733-1741, May 2015
- [21] A. Keshtkar, "Effect of rail dimension on current distribution and inductance gradient," IEEE Trans. Magn., vol. 41, no. 1, pp. 383–386, Jan. 2005.

- [22] Siaenen, T.; Schneider, M.; Hogan, J., "Block Diagram Model for the Simulation of an Electromagnetic Rail Accelerator System," in Plasma Science, IEEE Transactions on , vol.43, no.5, pp.1580-1584, May 2015
- [23] Conventional Space Weapons [Online]. Available: [http://www.projectrho.com/public\\_html/rocket/spacegunconvent.php](http://www.projectrho.com/public_html/rocket/spacegunconvent.php) (last accessed on 30 November 2015)
- [24] Allen S. Feliciano, "The Design and Optimization of a Power Supply for a One meter Electromagnetic Railgun," Master's thesis, Naval Postgraduate School, Monterey, California, December 2001.
- [25] J. F. Kerrisk, "Current Distribution and Inductance Calculations for Rail-gun Conductors," Report No. LA -9092-Ms, Los Alamos National Laboratory, Nov.1981
- [26] M. Coffo, J.Gallant. "Modelling of a parallel augmented railgun with PSpice validation of the model and optimization of the augmenting circuit," PPPC Conference, 2007:18-22
- [27] Yuan Zhou; Dongdong Zhang; Ping Yan, "Modeling of Electromagnetic Rail Launcher System Based on Multifactor Effects," in Plasma Science, IEEE Transactions on , vol.43, no.5, pp.1516-1522, May 2015
- [28] F. J. Deadrick, R. S. Hawke, and J. D. Scudder, "MAGRAC – A Railgun Simulation Program," IEEE Transactions on Magnetism, vol. 18, no. 1, 1982.
- [29] Xinjie Yu; Zhaonan Fan, "Simulation and Two-Objective Optimization of the Electromagnetic-Railgun Model Considering VSEC Resistance and Contact Resistance," in Plasma Science, IEEE Transactions on , vol.39, no.1, pp.405-410, Jan. 2011

- [30] Sengil, N., "Implementation of Monte Carlo Method on Electromagnetic Launcher Simulator," in Plasma Science, IEEE Transactions on , vol.41, no.5, pp.1156-1160, May 2013
- [31] Xiaolong Guo; Ling Dai; Qin Zhang; Fuchang Lin; Qinghua Huang; Tingzhi Zhao, "Influences of Electric Parameters of Pulsed Power Supply on Electromagnetic Railgun System," in Plasma Science, IEEE Transactions on , vol.43, no.9, pp.3260-3267, Sept. 2015
- [32] Yuan Zhou; Dongdong Zhang; Ping Yan; Weiqun Yuan, "Circuit simulation research of electromagnetic rail launcher system with a view to multi-field characteristics," in Electromagnetic Launch Technology (EML), 2014 17th International Symposium on , vol., no., pp.1-6, 7-11 July 2014
- [33] Bernardes, J.S.; Stumborg, M.F.; Jean, T.E., "Analysis of a capacitor-based pulsed-power system for driving long-range electromagnetic guns," in Magnetics, IEEE Transactions on , vol.39, no.1, pp.486-490, Jan. 2003
- [34] J. Wey, E. Spahn, M. Lichtenverger. "Railgun modelling with the P-Spice code,". IEEE Trans. Magn., 1997, 33(1): 619-624
- [35] DS W. F. Ray, C. R. Hewson, "High performance Rogowski current transducers," Conference Record of the 2000 IEEE Industry Applications Conference, vol. 5, pp. 3083 – 3090, 2000.



## APPENDIX A

### ROGOWSKI COIL DATASHEET

## CWT SPECIFICATION

The **CWT** from *Power Electronic Measurements Ltd.* is a state of the art wide-bandwidth ac current probe.

The CWT is ideal for power electronics development work because it combines an easy to use thin, flexible, clip-around coil with an ability to accurately replicate fast switching current waveforms be they sinusoidal, quasi-sinusoidal or pulsed.

A 2700A current pulse with a 6700A/µs falling edge measured by a CWT15 with a 500mm coil and a very high bandwidth coaxial shunt - 10µs/div.

## PERFORMANCE CHARACTERISTICS

| Type | Sensitivity<br>(mV/A) | Peak<br>current<br>(kA) | Peak<br>di/dt<br>(kA/μs) | Noise<br>max <sup>1</sup><br>(mV <sub>rms</sub> ) | Droop<br>typ.<br>(%/ms) | LF (3dB)<br>bandwidth<br>typ. (Hz) f <sub>L</sub> | Phase lead<br>at 50Hz<br>typ. (deg) | HF (3dB) bandwidth<br>typ. (MHz) f <sub>H</sub> <sup>2</sup> |                      |
|------|-----------------------|-------------------------|--------------------------|---|-------------------------|---|-------------------------------------|--|----------------------|
|      |                       |                         |                          |   |                         |   |                                     | Coil Length<br>300mm   | Coil Length<br>700mm |

### High Sensitivity Ranges of CWT ... measuring currents from 300mA

|        |       |      |     |     |     |     |             |    |     |
|--------|-------|------|-----|-----|-----|-----|-------------|----|-----|
| CWT015 | 200.0 | 0.03 | 0.2 | 6.5 | 130 | 150 | 2.0 @ 6kHz  | 6  | 4   |
| CWT03  | 100.0 | 0.06 | 0.4 | 4.5 | 90  | 105 | 2.0 @ 4kHz  | 10 | 6.5 |
| CWT06  | 50.0  | 0.12 | 0.8 | 3.0 | 70  | 80  | 2.0 @ 3kHz  | 16 | 10  |
| CWT1   | 20.0  | 0.3  | 2.0 | 2.5 | 40  | 50  | 1.9 @ 2kHz  | 16 | 10  |
| CWT1N  | 20.0  | 0.3  | 2.0 | 2.0 | 20  | 25  | 1.9 @ 1kHz  | 10 | 5   |
| CWT3   | 10.0  | 0.6  | 4.0 | 8.0 | 3.0 | 3.5 | 1.0 @ 300Hz | 16 | 10  |

### Standard Ranges of CWT ... measuring currents from 15A

|         |      |       |      |      |       |      |      |    |    |
|---------|------|-------|------|------|-------|------|------|----|----|
| CWT3N   | 10.0 | 0.6   | 4.0  | 14.0 | 0.9   | 1.0  | 1.7  | 10 | 5  |
| CWT6    | 5.0  | 1.2   | 8.0  | 14.0 | 0.9   | 1.0  | 1.7  | 16 | 10 |
| CWT15   | 2.0  | 3.0   | 20.0 | 7.0  | 0.7   | 0.8  | 1.3  | 16 | 10 |
| CWT30   | 1.0  | 6.0   | 40.0 | 5.0  | 0.5   | 0.6  | 0.9  | 16 | 10 |
| CWT60   | 0.5  | 12.0  | 40.0 | 3.5  | 0.35  | 0.4  | 0.6  | 16 | 10 |
| CWT150  | 0.2  | 30.0  | 40.0 | 3.0  | 0.2   | 0.2  | 0.3  | 16 | 10 |
| CWT300  | 0.1  | 60.0  | 40.0 | 3.0  | 0.1   | 0.1  | 0.2  | 16 | 10 |
| CWT600  | 0.05 | 120.0 | 40.0 | 3.0  | 0.06  | 0.05 | 0.1  | 16 | 10 |
| CWT1500 | 0.02 | 300.0 | 40.0 | 3.0  | 0.035 | 0.03 | 0.06 | 16 | 10 |

<sup>1</sup> Distributed around the f<sub>L</sub> (-3dB) bandwidth.

<sup>2</sup> For 2.5m cable length. Contact PEM for values of f<sub>H</sub> for other coil and cable lengths

|                         |   |                          |                     |
|-------------------------|---|--------------------------|---------------------|
| <b>TYPICAL ACCURACY</b> | Traceable calibration to ±0.2% with conductor central in the loop<br>Variation with conductor position in the coil loop typically ±1% | <b>TYPICAL LINEARITY</b> | ±0.05% (Full Scale) |
|-------------------------|---|--------------------------|---------------------|

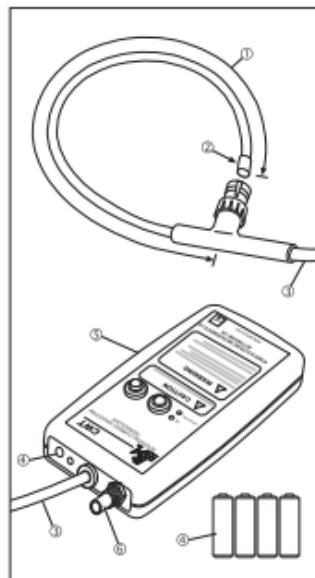
|   |  |  |   |  |
|---|--|--|---|--|
| <b>ABSOLUTE MAXIMUM VALUES OF di/dt (kA/μs)</b><br>(value must not be exceeded) | CWT 03, 06<br>CWT 015, 1N, 3N<br>all other CWT's | <b>PEAK</b> 40.0<br><b>PEAK</b> 20.0<br><b>PEAK</b> 40.0 | <b>RMS</b> 1.2 @ 70°C<br><b>RMS</b> 1.0 @ 70°C<br><b>RMS</b> 1.5 @ 70°C | (Further information available on request) |
|---|--|--|---|--|

## COIL AND CABLE

|  |                             |
|--|-----------------------------|
| ① COIL CIRCUMFERENCE   | 300, 500, 700 or 1000mm     |
| ② COIL CROSS SECTION (max)   | 8.5mm - (14 mm with sleeve) |
| <b>PEAK COIL VOLTAGE ISOLATION</b>   | 10kV                        |
| Safe peak working voltage to earth. The coils are flash tested at 15kVrms for 60 seconds. The coil is supplied with a removable silicone sleeve which provides additional mechanical protection. Information about continuous use of the coils at high voltage can be obtained from PEM. |                             |
| <b>TEMPERATURE RANGE</b>   | -20°C to 100°C              |
| For de-rating due to temperature cycling please consult PEM  |                             |
| ③ CABLE LENGTH (from box to coil)  | 2.5m or 4m                  |

## INTEGRATOR

|  |  |
|--|--|
| <b>④ POWER SUPPLY</b>  |  |
| <b>B</b> Battery 4 x AA (1.5V standard alkali batteries)<br>-plus-<br>2.1/2.5mm socket for 12 to 24V (±10%) DC input<br><br>Typical life 70hrs<br>Battery inoperative with DC supply present | <b>R</b> Rechargeable battery 4 x AA (rechargeable NiMH batteries)<br>-plus-<br>2.1/2.5mm socket for 12 to 24V (±10%) DC input<br><br>Recharge time 40hrs, Typical life 30hrs<br>Battery is charged whenever DC supply present |
| <b>⑤ INTEGRATOR BOX DIMENSIONS</b>   | H = 183mm, W = 93mm, D = 32mm  |
| <b>⑥ OUTPUT SOCKET</b>   | BNC (output impedance 50Ω) - unit supplied with 0.5m BNC - BNC coaxial cable)  |
| <b>MIN. OUTPUT LOADING</b>   | 100kΩ (for rated accuracy)   |
| <b>TEMPERATURE RANGE</b>   | 0°C to 40°C  |



## **APPENDIX B**

### **SIMULINK BLOCK DIAGRAM MODEL**

## BLOCK DIAGRAM MODEL FOR MULTISTAGE EML

